How fast can minibasins translate down a slope?
Observations from 2D numerical models

Naiara Fernandez[1]*, Oliver B. Duffy[1], Christopher A-L. Jackson[2,3], Boris J.P. Kaus[4], Tim Dooley[1], Michael Hudec[1]

[1]*Bureau of Economic Geology, Jackson School of Geosciences, The University of Texas at Austin, University Station, Box X, Austin, Texas, 78713-8924, USA*

[2]*Basins Research Group (BRG), Department of Earth Science & Engineering, Imperial College, Prince Consort Road, London, United Kingdom, SW7 2BP, UK*

[3]*Jacobs, 5 First Street, Manchester, M15 4GU, UK*

[4]*Institute of Geosciences, Johannes Gutenberg University Mainz J.-J.-Becher-Weg 21, D-55128 Mainz, Germany*

**Now at Helmholtz Centre Potsdam GFZ – German Research Centre for Geosciences*

Corresponding author: naiara@gfz-potsdam.de

Running Title: Minibasin Translation

Keywords: salt tectonics; salt-detached slopes; continental slopes; salt velocity; minibasin translation;

1. Abstract

Minibasins are important features in salt-bearing basins and are abundant in salt-detached continental slopes where the salt and the overlying sedimentary cover (including minibasins) undergo seaward translation due to gravity. The gravity-driven translation of salt exerts an important control on the structural style and depositional systems distribution on continental slopes. Estimates of translation velocity of the salt and the overlying cover over geological times rely on indirect observations that are scarce. One question which is relevant for understanding the structural evolution of salt-detached slopes is what controls the translation velocity of the salt layer and of the overlying sedimentary cover (and minibasins). The aim of this study is three-fold: 1) to compare minibasin downslope translation velocity with salt translation velocity; 2) to understand what controls minibasin translation velocity and 3) to understand how minibasins translating at different velocities can kinematically interact and modify strain patterns around them. To address these questions, we present a 2D numerical modelling study consisting of three simulation series. In the first series, we model a simple scenario where, as a result of gravity, a constant-thickness salt layer moves downslope on an inclined plane. In the second series, we use the same model geometry as in the first (i.e. constant thickness salt layer over an inclined plane), but we add a single, isolated minibasin at the updip portion of the slope. Different minibasin thicknesses, widths and densities are then tested, replicating how in natural salt basins, minibasin size (thickness and width) and fill (density as a proxy of lithology) vary as a function of their maturity, their structural position, and/or the overall regional geological setting in which they form and evolve. Finally, in the third model series, we add three minibasins to the updip portion of the slope, and assess how they interact as they translate downslope. In addition to parameters that control salt velocity on a slope, we show that minibasin thickness is the main factor controlling minibasin velocity in the numerical models. More specifically, thicker minibasins translate slower than thinner minibasins. Findings from our numerical modelling provide additional conceptual understanding of structural evolution of salt-detached continental slopes that have significant implications for understanding minibasin behaviour, and interpreting kinematics and strain patterns around them.

1. Introduction

Minibasins are important features of many salt-bearing basins. Minibasins are small synkinematic basins that form by subsidence into a relatively thick layer of salt (Jackson and Talbot, 1991). They can form in different geodynamic settings (e.g., rift basins, foreland basins) and many are found on salt-detached slopes formed along continental margins (e.g. Jackson and Hudec, 2017). One characteristic of salt-detached slopes is the seaward translation of the salt and its overlying sedimentary cover. Over geological time scales, salt behaves as a viscous fluid. As a result, on salt-bearing continental slopes salt moves downslope due to gravity in response to two main driving mechanisms: gravity spreading (deformation and collapse of a rock mass by its own weight) and gravity gliding (downslope translation of the rock mass over an inclined detachment) (e.g. De Jong and Scholten, 1973; Ramberg 1981; Brun and Merle, 1985). Distinguishing between these mechanisms on natural continental slopes is difficult, given it is likely that both processes contribute to the downslope flow of salt (e.g. Schulz-Ela, 2001; Rowan, 2004; Brun and Fort, 2011, 2012; Peel, 2014; Ge et al., 2019a, b). In both cases, as salt flows downslope the capping sedimentary cover on top also translates. One of the main outcomes of this style of salt-related deformation is the partitioning of continental slopes into three different domains: an up-dip extensional domain and a down-dip contractional domain, separated by a translational domain (Figure 1a and b).

Gravity causes salt (and overlying sedimentary cover) to flow down a slope, but how fast does salt move? Direct observation of salt flow is restricted to areas where salt is exposed at the Earth's surface, such as in Iran, where aerial extrusions from salt diapirs form salt glaciers (e.g. Lees, 1927; Kent, 1958; Wenkert, 1979). These well-exposed salt structures have enabled direct measurements of lateral salt flow at observational time scales (i.e., days to years), using, for example, geomorphological observations and surveys (Wenkert, 1979; Talbot and Rogers, 1980; Talbot and Javis, 1984; Talbot et al., 2000). In more recent years, satellite based interferometric synthetic aperture radar (InSAR) time series analysis has provided further insights into the uplift and lateral flow rate salt in some of these well-exposed salt structures (e.g. Aftabi et al., 2010; Ghassemi and Roustaei, 2020; Mohammadnia et al., 2021; Zhang et al., 2021). Lateral salt displacement values reported in such studies range from <1 to 400 cm/yr. However, subaerial salt flow responds to complex dissolution-precipitation processes that change the rheology of the salt, which means short-term salt flow rates cannot be directly extrapolated to salt flow over geological

time scales (10^3-10^6 years) (e.g. Urai et al., 1984; Zhang et al., 2021). In addition, salt extrusion associated with the Iranian salt diapirs is driven by tectonic shortening, which directly impacts and controls the rate of salt extrusion and lateral flow. Thus, our understanding of the rate of gravity driven salt flow at geological time scales and at regional scale (i.e. continental slope scale) remains poor.

In the case of salt-detached slopes, the velocity of salt flow in the geological past can be estimated by indirect observations. For example, in the northern Gulf of Mexico salt canopy, estimation of salt velocities come from the analysis of seismic reflection data. More specifically, this technique requires the assessment of age-constrained stratigraphic cut-offs at the base-of-salt over which the salt was advancing at the same time new sediments were being deposited in front of the advancing salt (e.g. Tauvers, 1993). Advance rates of salt sheets using structural restorations of geological sections constructed from seismic interpretations provide long-term advance or flow rates of 0.1-2 cm/year (e.g. Diegel et al., 1995, Peel et al., 1995; Schuster et al., 1995; Jackson and Hudec, 2017 and references therein). More recently in the Levant Basin (Eastern Mediterranean), fluid escape pipes transecting the mobile salt layer have been used to estimate an average salt velocity of 0.2 cm/year for a period of 1.7 myrs. (Cartwright et al., 2018). These attempts to constrain salt flow at geological time scales, based on natural examples, provide values that are 2-3 orders of magnitude slower than the ones directly measured in subaerial salt glaciers.

If constraining how fast salt moves at geological time-scales (thousands to millions of years) is challenging and has many uncertainties, constraining the translation velocity of the sedimentary cover that overlies salt is even more so. Compared to the updip extensional and the downdip compressional domains, clear indicators of displacement magnitudes (e.g. fault cutoffs) are usually absent in the translational domain (e.g. Jackson and Hudec, 2005). This is even more true if instead of a continuous cover, the translational domain is populated with minibasins that are only partially interconnected, as is the case of minibasin provinces located in continental slopes (e.g. Lower Congo Basin, Figure 1b; Northern Gulf of Mexico; Figure 1c). It is not unusual for velocity estimates of the sedimentary cover in the translational domains, to be inferred from observations of salt-detached ramp syncline basins and/or rafted minibasins (e.g. Jackson and Hudec, 2005; Jackson et al., 2010; Fiduk et al., 2014; Pilcher et al., 2014; Pichel et al., 2018; 2020; Evans and Jackson, 2021a, b; Fernandez et al., 2021). Estimates of the translation rate of sedimentary cover based on reconstructed cross-sections provide velocities in the ranges of 0.1-4

cm/year (e.g. rafted minibasins in the Gulf of Mexico: e.g. Jackson et al., 2010; ramp synclines in eastern Mediterranean: e.g. Evans et al., 2021a, b). However, minibasin translation velocities are presumably the result of the lateral salt flow in which they are transported and their own vertical subsidence into salt. It is also presumed that minibasin translation rates will dramatically decrease as they are close to welding at their base (e.g. Wagner and Jackson 2011). Furthermore, the downslope translation of minibasins can be obstructed by base-salt relief or friction associated with primary welding, processes that result in locally complex strain patterns of the sedimentary cover (e.g. Krueger, 2010; Duffy et al., 2020). Further complications arise from the fact that coevally subsiding minibasins can mutually alter their subsidence patterns and rates (e.g. Fernandez et al., 2020), potentially also affecting their translation velocities.

One question that has not been explicitly addressed before is, how different is the velocity of downslope-flowing salt from the velocities of overlying minibasins? More specifically, do minibasins translate at different velocities? If so, does minibasin thickness, geometry and density affect how fast they translate before they weld? Understanding if, why, and how salt and minibasins move at different velocities is relevant for understanding the structural evolution of salt-detached slopes. Ultimately, the absolute distance a minibasin can travel on a slope is constrained by its maximum translation velocity, as well as the time over which the translation could occurs. Thus, having a better understanding of what controls minibasin translation velocity will help constrain structural restorations of salt basins. Furthermore, if minibasins translating at different velocities coexist on a slope, this can result in differential translation between minibasins and may help explain the complex strain patterns around minibasins that are characteristics some salt-detached slopes (e.g. Krueger, 2010; Duffy et al., 2020; Fernandez et al., 2021).

The aim of this study is thus three-fold: 1) to compare minibasin downslope translation velocity with salt translation velocity; 2) to understand what controls minibasin translation velocity; and 3) to understand how minibasins translating at different velocities can kinematically interact and modify strain patterns on the slope. To achieve this goal, we undertake 2D numerical modelling consisting of three simulation series. In the first series, we model a simple scenario where, as a result of gravity, a constant-thickness salt layer moves downslope on an inclined plane (Figure 2a). This scenario reflects a simplification of the translational domain of a salt-detached continental slope (Figure 1a). For this particular scenario, an analytical solution already exists (e.g. Turcotte and Schubert, 2001), which we use to benchmark our numerical models. In the second

series, we use the same model geometry as in the first (i.e. constant thickness salt layer over an inclined plane), but we add a single, isolated minibasin at the updip portion of the slope. Different minibasin thicknesses, widths and densities are then tested, replicating how in natural salt basins, minibasin size (thickness and width) and sedimentary fill (density as a proxy of lithology) vary as a function of their maturity, their structural position, and/or the overall regional geological setting in which they form and evolve. Given that minibasins are rarely found in isolation, in the third simulation series, we add an array of three minibasins in the updip portion of the slope, and we assess how they interact as they translate downslope. The goal of this study is not to model a specific natural example. Rather, our objective is to identify the key principles and controls of salt flow and minibasin translation velocities at geological time-scales on salt-detached slopes. The values given are not intended to be taken as absolute values of velocity, but instead to provide a self-consistent framework to understand the relative impact of different parameters (e.g., slope angle, salt thickness, minibasin thickness and minibasin density) in minibasin translation velocity. However, when appropriate, comparisons with velocities reported in natural examples in the literature are provided throughout the text.

2. How fast does salt flow down a slope?

We are first interested in understanding regional-scale salt flow on salt-detached slopes. We can consider the salt-detached slope as equivalent to an inclined plane overlain by a viscous fluid layer of constant thickness (e.g. Turcotte and Schubert, 2001). The inclined plane would be analogous to the slope, and the viscous layer would be analogous to the salt (Figure 1 and 2a). A schematic diagram of the setup is shown in Figure 2a, where, **u** is velocity, **ρ** is salt density, **μ** is salt viscosity, **g** is gravity, **α** is the slope angle and **h** is the salt layer thickness.

Using a fluid dynamics approach, the velocity profile of the unidirectional flow of a viscous fluid down an inclined plane can be obtained assuming the following conditions: the flow occurs in a layer of constant thickness (h) viscous fluid; no-slip condition (u = 0) at y=h; and free-surface (τ = 0) condition at y=0.

$$u = \frac{\rho g \sin \alpha}{2\mu}(h^2 - y^2) \qquad (1)$$

The equation can be solved for the maximum and mean velocity in the layer, and we obtain:

$$u_{max} = \frac{\rho g \sin\alpha}{2\mu}(h^2) \quad (2)$$

$$u_{mean} = \bar{u} = \frac{\rho g \sin\alpha}{3\mu}(h^2) \quad (3)$$

Derivations of the equations Eq. (1), Eq. (2) and Eq. (3) are described in Appendix A. These equations can be used to calculate both the maximum and mean velocity of the salt on a salt-detached slope, if we use the appropriate values for the parameters (within the ranges observed in the natural examples described above). A normalized analytical velocity profile can be obtained from Eq. (1) by plotting it in the non-dimensional y/h and u/u_{max} axes (Figure 2b). The maximum velocity occurs at the surface of the salt, where y = 0 and the velocity is zero at y=h (Figure 2b). The average value of the salt velocity profile corresponds to $u_{mean} = \frac{2}{3} u_{max}$. Eq. (1) is also used to perform calculations for a combination of the main parameters: salt thickness and slope angle. We use a range of salt thicknesses (0.1-4 km) and slope angles (0.1-4°) that covers ranges comparable to those encountered on natural salt-detached continental slopes (e.g. Peel, 2014 and references therein). Salt density is taken to be 2200 kg m^{-3}, an appropriate value for a halite salt-rock with 5% of impurities (e.g. Gevantman, 1981; Jackson and Hudec, 2017). The rheology of salt at geological time scales is still widely debated and depends on many factors, including the tectonic setting (e.g. Urai et al., 2008.; Jackson and Hudec, 2017). While a non-linear rheology of salt has been argued for a tectonically inactive setting without salt flow (e.g. Li et al., 2012), recent numerical models have argued in favour of a linear-viscous rheology of salt in extensional settings (Granado et al., 2021). In this study, we model the salt as a linear-viscous material characterised by a viscosity of 10^{18} Pa s (e.g. Mukherjee et al., 2010 and references therein). Assuming a linear-viscous rheology of the salt is a simplification that facilitates comparison with the simple analytical solution outlined above. The mean and maximum salt velocities calculated analytically for the given parameter ranges are plotted in Figure 3 (maximum velocity contours represented by solid lines, mean velocity contours by dashed lines). For example, for a salt layer of 2 km thickness, with a slope angle of **α =** 2° (grey circle, Figure 3), the maximum salt velocity is 4.75 cm/year and the mean salt velocity is 3.17 cm/year. For the same slope angle of 2°, but a salt-layer thickness of 4 km, the maximum predicted velocity is 18.99 cm/year at the top of the salt layer, whereas the predicted mean salt velocity is 12.66 cm/year. For a salt thickness of 2 km, but with a slope angle of 1°, the maximum predicted velocity is 2.375 cm/year at the top of the salt layer, whereas the predicted mean salt velocity is significantly lower, at 1.58 cm/year. The analytical results illustrate

that salt flows faster with increasing slope angle and increasing salt thickness (see Eqs. 2 and 3 and Fig. 3). If we consider slope angles of 0.5 to 1° and a salt layer thickness of 1-1.5 km (i.e., comparable to the Levant Basin, eastern Mediterranean; Cartwright et al., 2018), the maximum salt velocity is 0.3-1.3 cm/year and the mean salt velocity 0.2-0.9 cm/year, which is of a similar order of magnitude to the local estimate of salt velocity estimated from kinematic indicators (e.g. Cartwright et al., 2018). This adds confidence that the analytical solution appears to broadly capture the actual physics occurring in natural examples.

The analytical solution serves as a benchmark for our numerical experiments (see below). We use the 2D finite-element code MVEP2 (Kaus, 2010; Thielmann & Kaus 2012; Johnson et al. 2013). MVEP2 solves the equations of conservation of mass and momentum for incompressible materials with visco-elasto-plastic rheologies, and employs Matlab-based MILAMIN approach (Dabrowski et al. 2008) for efficiency. The code uses a Lagrangian approach, where material properties are tracked by randomly distributed markers that are advected according to the velocity field that is calculated in a deformable numerical grid. Remeshing of the grid is performed every time step. The method and numerical implementation are explained in detail in Kaus (2010).

The numerical model domain is a 120 km-long, 10 km-high modelling box (Figure 4a). All the boundary conditions of the modelling box are set to free-slip (velocity is parallel to the boundary). The initial geometry within the model box consists of an inclined basement capped by an undeformed salt layer of constant thickness (Figure 4a). The top of salt is modelled as an internal free surface along which relief can develop. In numerical simulations with this initial geometry, salt will immediately flow downslope due to gravity, causing salt to thicken at the base of the slope, and thin at the upper slope (Figure 4b). To keep the thickness of salt constant, an internal boundary condition has been applied to the interface between the salt and the air/water (Figure 4c and d). The aim of the internal boundary condition is to ‘remove’ salt flowing above the initial inclined topography at the base of the slope, and ‘add’ salt to fill in the area at the top of the slope depleted of salt below the initial topographic level (Figure 4d). This boundary condition ultimately produces a continuous flow of salt on the slope, keeping the salt thickness constant such that it is comparable to the scenario for which the analytical solution exists (compare Figure 2a and Figure 4c). The variables tested in these numerical simulations are the following: inclination of the slope (α), salt viscosity (μ) and density (ρ) and thickness of salt layer (h). The results of numerical experiments are compared with the predictions of the analytical solution to test the appropriateness

of the numerical simulations (Figure 2b). Velocity profiles obtained from numerical simulations with constant salt thickness plot on top of, or very close to, the velocity profile obtained analytically (Figure 2b). With a resolution of 1000 X 100 element nodes (element size of 120 m x 100 m), the deviance of the numerical solution from the analytical solution is ~1 %.

The central portion of the slope in the numerical simulations (between -40 km to 40 km) has a salt velocity profile that remains constant through time, not influenced by edge or boundary effects resulting from the applied internal boundary condition (Figure 4c). Thus, we consider this portion of the numerical domain to be an appropriate representation of an ideal translational domain of a continental slope (Figure 1a). In such an idealized domain, the effects of the updip extensional and downdip compressional domains are far enough away as not to affect the dynamics of salt flow and translation (Figure 4c). Herein, we will focus on the central portion of the slope.

3. How fast do Minibasins Translate Downslope?

The series of numerical simulations described in this section are aimed at understanding what controls the downslope translation velocities of minibasins on a salt-detached slope. The geometry of the numerical models is the same as the one used to reproduce the analytical solution of salt flowing on an inclined plane (Figure 3a). However, in this series a single isolated minibasin is added to the upper slope in each of the simulations. Although minibasins are rarely isolated in nature, these simulations aim to develop an understanding of the fundamental controls on minibasin downslope translation, in the absence of neighbouring minibasins. It is also important to note that the minibasins used in the simulations approximate rounded-at-the-base semi-circles to minimize the effect of the basal viscous drag, whose effect is discussed later. Two model sub-series are described in this section: 1) one in which the density of the minibasins is equal to that of the salt (i.e. neutral-buoyancy minibasins); the aim of this sub-series is to understand the effect of minibasin geometry (mainly thickness and width) on their translation velocity, and; 2) one in which the minibasin density differs from the salt, such that the minibasin either subsides (i.e. minibasins are denser than salt) or rises (i.e. minibasins are less dense than salt) as it translates downslope.

We have performed simulations with a salt viscosity (μ_{salt}) of 10^{18} Pa s, salt a density (ρ_{salt}) of 2200 kg/m^3, slope angles (α) of 2°-4°, and a salt thickness (H_{salt}) of 2-4 km. However, we only describe here the results of simulations with a slope angle of 2° and a salt thickness of 2 km, value

that are within the range of those reported for different natural examples of salt-detached slopes (simulations with a slope angle of $\alpha = 2°$ and H_{salt}= 4 km are discussed in supplemental material). The minibasins in the numerical simulations are modelled as being visco-plastic following the Drucker-Prager yield criterion. The minibasins are characterized by a friction angle (ϕ) of 30°, and a cohesion (C) of 20 MPa, relatively competent material, to avoid internal deformation as they translate. Simulations are run for several hundreds of time-steps. The last time-steps are discarded and are not described here, because as the minibasins approach the base of the slope they get closer to the area where the effects of the applied internal boundary conditions influence the salt velocity. For each of the simulations the velocity field calculated in the code is used to extract the translation velocity of the minibasin at each time-step. Next, we describe the observations from each model sub-series.

3.1 Models with Neutral-Buoyancy Minibasins

In models containing neutral buoyancy minibasins, $\rho_{minibasin} = \rho_{salt} = 2200$ kg/m^3, minibasins translate downslope with the flowing salt. As the density of the minibasins is equal to that of the salt, they do not subside into or rise above salt (Figure 5, also Figure S1). After around 1,000,000 years, the minibasins have traversed the central portion of the slope (Figure 5).

We now explore the effect of minibasin thicknesses. The initial thickness of the three minibasins considered is either 900 m (herein referred to as 'thin' minibasin) or 1250 m (herein referred to as 'thick' minibasin). These values correspond to minibasin thickness (T_{mb}) to salt thickness (H_{salt}) ratios of $T_{mb}/H_{salt} \sim 0.425$ and 0.625. If different minibasin thickness to salt thickness ratios are used, we specify in the text. Images of the simulations are shown for the initial geometry and for two time-steps, after ~500,000 and ~1,000,000 years, along with their corresponding velocity plots (Figure 5a, b). Our results show that the thin minibasin translated further downslope than the thick minibasin during the same time interval (compare Figure 5a and 5b). The translation velocity of neutral buoyancy minibasins remains nearly constant throughout the simulation (Figure 5c, d). The mean velocity of the minibasins during this translational stage is 3.52 cm/year and 4.09 cm/year, for the thick and thin minibasins, respectively (Figure 5c, d). Thicker minibasins translate at lower velocities. When compared to the velocity obtained for salt (i.e. 4.75 cm/year maximum salt velocity; 3.17 cm/year mean salt velocity), we note that minibasins translate at a velocity lower than the theoretical maximum salt velocity (Eq. (2)).

However, whereas the thick minibasin translates at a velocity lower than the theoretical mean salt velocity (Eq. (3)), the thin minibasin translates faster than the theoretical mean salt velocity.

The effect of the free surface that allows for the build-up of salt topography in the central part of the models is best noticed in a simulation with thicker salt (e.g. 4 km) and slope angle of 2° when compared to the simulation where no salt topography is allowed to develop (Figure S2).

3.2 Models with Subsiding and Buoyant Minibasins

In models where minibasins have a density different to that of the salt, they will either subside into salt (if denser than salt) or rise buoyantly (if less dense than salt) as they translate downslope. A snapshot after the same time interval in simulations with subsiding and buoyant thick and thin minibasins is shown in Figure 6 (also Figure S3). The minibasins in the Figure have density values of $\rho_{minibasin}$ = 2000, 2100, 2200 2300, 2400, and 2500 kg/m^3 (salt density being ρ_{salt} = 2200 kg/ m^3). Our models show that, unsurprisingly, the denser the minibasin, the faster it subsides into salt. In our simulations, sediment fills the accommodation created as a minibasin subsides. Accommodation in downslope-translating minibasins is invariably created on the up-dip side of the minibasin. By the end of the simulation, the minibasins are overlain by a wedge-shaped sediment package that thickens up-dip (light brown colour wedge shapes seen in Figure 6). The systematic updip orientation of the wedge-shaped sediment package arises from the simple geometry of the model setup, where single, isolated minibasins are subsiding into salt flowing down a smooth base of salt. The denser the minibasin is initially, the thicker the final wedge-shaped package is at the end of the simulation (Figure 6). When the results of simulations with minibasins of different densities are compared at the same time step, it can be observed that the amount of distance travelled by the minibasins differs (Figure 6). The denser the minibasin, the shorter its translation distance (Figure 6). As expected from the experiment with neutral-density minibasins of the previous section, the thinner minibasins, which in this case are the less dense ones, translated further.

We can further assess the effect of density on minibasin translation velocity by looking at temporal changes in velocity (Figure 7, also Figure S4). This shows that subsiding minibasins tend to decrease their translation velocity as they subside and become thicker (Figure 7). Conversely, buoyant minibasins tend to increase their velocity through time as they rise over salt (Figure 7).

However, the temporal *increase* of translation velocity in buoyant minibasins is small compared to the velocity *decrease* through time associated with subsiding minibasins (Figure 7).

4 What controls minibasin velocity?

As minibasins in the simulations are embedded in the flowing salt, the first-order control on minibasin velocity in the absence of any other external factor (i.e. tectonics) is presumably the velocity of the flowing salt. A theoretical salt velocity profile, and its corresponding maximum and mean salt velocities can be calculated from the analytical solution (Eq. (1); Figure 2 and Eq. (2) and (3); and Appendix A). However, that analytical solution is a 1D channel flow approximation, where there is no shear stress variation in the direction parallel to the slope (see Appendix A for details). Given this constraint, we now discuss how the thickness (normalized over salt thickness) and aspect ratio of minibasins affect their translation velocity, and how this relates to the analytically predicted salt velocity.

The sketch in Figure 8 illustrates a constant thickness salt layer on a slope with a minibasin embedded in the salt. The thickness of the minibasins at its centre is T_{mb}, thus, the basal position of the minibasin in a y-axis profile would correspond to $y = T_{mb}$. This position ($y= T_{mb}$) can be used to conceptually divide the salt layer profile into two different portions: an upper salt portion, from 0 to $y= T_{mb}$, and a lower salt portion, from $y= T_{mb}$ to y=h. Various theoretical salt velocity profiles (and corresponding maximum and mean values) can be calculated considering the salt layer to be split into two portions at $y= T_{mb}$. The theoretical profiles are illustrated in Figure 8.

The analytical salt profile described by Eq. (1) can be used to calculate the theoretical salt velocity profile for the complete salt layer (thickness h). Then, the mean salt velocity of the upper portion of this entire salt velocity profile can be calculated and we will refer to this mean velocity as, $\underline{u}_{mb}$. Similarly, Eq. (1), can be used to obtain the mean velocity of a theoretical salt velocity profile of the upper salt portion ($h'=y=T_{mb}$). We refer to this mean velocity as $\underline{u}$. The corresponding mathematical expressions of these definitions are described in detail in Appendix A.

Next, we compare the results from the numerical simulations of minibasin translation, with these analytically-predicted, mean velocity profiles.

4.1 Minibasin Thickness

Numerical simulations with neutral buoyancy minibasins of different thicknesses have been used to extract the minibasin velocity after the initial time-step, for three different initial model geometries (H=4 km and α = 4°; H=4 and α = 2°; H=2 and α = 4°). Given that we have already demonstrated that the velocity of neutral buoyancy minibasins in the numerical models is approximately constant through time (see Figure 5), we have taken the value of one time-step in each simulation. Each numerical model result is plotted in Figure 9a. Numerically calculated velocities fall on one of the analytically calculated lines (Figure 9a). Thus, the velocity of neutral buoyancy minibasins for minibasin whose thickness is less than 70% of the total salt thickness is described by the following equation (check Appendix A for details):

$$u_{mb} = u_h - \underline{u}_{y=Tmb} = \frac{\rho\, g\, sin\alpha\, h^2}{\mu\, 2} - \frac{\rho\, g\, sin\alpha\, y^2}{\mu\, 3} \quad (4)$$

It must be noted that minibasin velocity calculated from the numerical models deviates from the line described by Eq. (4) when the minibasin thickness approximates the salt thickness (minibasin thickness T_{mb}>70% H or T_{mb}/H_{salt} > 0.7) (Figure 9a). This implies that in the numerical models there is an effect of the base salt boundary on minibasin translation, an important feature not captured by the analytical solution. The effect of the proximity of the minibasin to the base-of-salt is to slow down the translation velocity (e.g. Wagner & Jackson, 2011).

Compared to neutral-density minibasins, we have seen that subsiding minibasins increase their thickness and decrease their translation velocity through time. We have plotted the evolution of thickness and corresponding minibasins velocity in numerical simulations with subsiding minibasins, for minibasins with a density = 2500 kg/m^3 (Figure 9b). The results of three numerical simulations with different initial minibasin thickness to salt thickness ratios of T_{mb}/H_{salt} ~0.325, 0.575 and 0.825 are shown in Figure 9b. Subsiding minibasins follow the analytical curve described by Eq. (6) as they increase their thickness. However, as for the neutral minibasins, the effect of the model base (base-of-salt) is to dramatically decrease minibasin translation velocity (Figure 9b). This more pronounced decrease in minibasin translation velocity occurs when subsiding minibasins reach a thickness that is close to that of the salt layer (>70%), at which point the model results deviate from the analytical solution of Eq. (6) (Figure 9b).

The graphs of Figure 9, can be used in conjunction with Eq. (1), to predict the minibasin velocities that would be expected in the numerical models, without actually performing new simulations. For a given minibasin thickness (normalized over salt thickness), from the graphs of Figure 9, we can obtain the minibasin velocity (normalized over maximum analytical salt velocity).

That normalized minibasin velocity can be converted to an "actual" velocity (e.g. cm/year) by using the analytical maximum salt velocity as calculated from Eq. (1). However, it must be noted that in the analytical solution and the numerical simulations discussed in the text, the top of salt is modelled as a subaerial free-surface. A salt-detached slope that is completely under water, is subjected to the additional load imposed by the water column, with the load increasing with salt depth downslope. The salt velocity in a slope covered with water would therefore be lower than for a subaerial slope, the effective difference between the velocities depending of the water column difference across the slope, which is related to the slope angle and slope length. We have checked the differences with a numerical simulation. For the example given earlier in Section 2 of a 2° slope and 2 km thickness salt, the mean salt velocity is 3.17 cm/year in a subaerial slope. Instead if the model domain is assumed to be filled with water of density 1000 kg/m^3 with depth increasing from 0 updip to 4.2 km downdip, the resulting mean velocity of salt due to gravity-driven flow is 2.49 cm/year. It is for this reason that minibasin velocities provided in the graphs of Figure 9 are normalized to the maximum salt velocity. The velocity of salt in a water covered slope depends on more parameters (mainly model domain length) that are not considered here for simplification but that may be worth exploring in the future.

4.2 Minibasin Aspect Ratio

As mentioned previously, the minibasins used in the simulations in Figs 5 and 6 are approximated as rounded-at-the-base semi-circles. This shape minimizes the effect of the basal viscous drag, as the contact surface in the direction of the salt flow, which is parallel to the slope, is almost infinitely small. Increasing the aspect ratio of the minibasins and making them wider increases the contact length between the minibasin and the base salt, thus increasing viscous drag and potentially reducing minibasin translation velocity (Figure 10a and Figure S5). We test this effect using numerical simulations of minibasins of different aspect ratios and basal lengths, noting small differences in their translation velocities (Figure 10a). Although, the overall effect of increasing minibasin aspect ratio is much less dramatic when compared to the effect of increasing minibasin thickness, it is notable in the case of thick minibasins. If a minibasin is thin and the effect of the base-of-salt is negligible (i.e. the kinematics can still be described by the dashed red curve given by Eq. (4), Figure 9a), the aspect ratio has almost no influence on translation velocity. For example, a thin minibasin with a thickness to salt thickness ratio of T_{mb}/H_{salt} ~0.325, is not influenced by the base-of-salt (Figure 9a, dashed red line). In such a case, increasing the minibasin

418 width to double the original width (factor of 2 increase), results in a <5 % decrease in translation
419 velocity (Figure 10b; line described by grey circles for T_{mb}/H_{salt} ~0.325). If instead, the initial
420 minibasin is thick and its velocity is already affected by the base-of-salt as described previously
421 (i.e. deviates from Eq. (4), Figure 10a), then changes in aspect ratio become more significant. For
422 example, for a minibasin with a T_{mb}/H_{salt} of ~=0.825, increasing minibasin width by a factor of 2.5
423 results in a 25% decrease in translation velocity (Figure 10b; line described by black stars for
424 T_{mb}/H_{salt} ~0.825). This effect can be explained by the we are increasing the surface of the minibasin
425 exposed to viscous drag.

426 5 Strain patterns around minibasins moving at different velocities

427

428 We have shown that neutral-density minibasins of different initial thicknesses translate at
429 different velocities. We have also shown that subsiding minibasins decrease their velocity as they
430 increase their thickness, as well as providing new intra-slope accommodation as they translate
431 downslope. Now we explore how minibasins interact as they translate downslope at different
432 velocities. Can the different translation velocities result in minibasins converging or diverging
433 from each other as they travel downslope? If so, how does this influence local strain patterns?
434 We can hypothesise that if a minibasin translates faster than another minibasin further
435 upslope of it, then over time, the distance between the two will increase. In contrast, if the upslope
436 minibasin is faster than the downslope minibasin, it follows that the opposite will occur and the
437 minibasins will converge and possibly collide. To test these hypotheses and illustrate the resulting
438 strain patterns around minibasins moving downslope at different velocities, we performed a final
439 series of numerical models comprising a chain of three neutral-density minibasins of different
440 thicknesses (Figure 11a, b, see also Figure S6). A thin minibasin located upslope (MB1) moves
441 downslope along with a thick minibasin (MB2) located further downslope, and a third thin
442 minibasin located even further downslope (MB2) (Figure 11a, b). The minibasins are separated by
443 diapirs labelled D1 and D2 in Figure 11a, b. Given this minibasin configuration, we test two
444 scenarios: one in which the diapirs between minibasins contain no roof, and other in which the
445 diapirs between the minibasins are overlain by a 200 m-thick roof of visco-plastic material that is
446 weaker (lower friction angle; $\phi = 15^{\circ}$ and lower cohesion; C = 5 MPa) than the minibasins (Figure
447 11a, b) to allow its deformation.

We first discuss the case with no roof over the diapirs. At the beginning of the simulation, the minibasins translate downslope (Figure 11a). The evolution of the velocity for each of the minibasins is shown in Figure 11c. MB1 and MB3, the thin minibasins, translate faster than MB2, the thick minibasin. Because the thinner minibasins are faster than the thicker one, the furthest downslope minibasin (MB3) diverges from the thick minibasin located just upslope (MB2). Conversely, the upslope minibasin MB1 converges with the thick minibasin and the intervening diapir is squeezed (Figure 11a). This convergence and divergence between the minibasins can be analyzed in terms of strain and strain rate, as calculated by the change in distance between the minibasins and is shown in Figure 12a. Convergence between the minibasins can occur because of the shortening accommodated by squeezing the intervening diapir, whereas the divergence must be accommodated by extension and widening of the intervening diapir. When the diapirs are not capped by a sediment roof, shortening and extension associated with converging and diverging minibasins is cryptically accommodated by the intervening salt. It would be very difficult to detect this deformation in natural systems. Once the minibasins have collided (circa 0.65 Myrs, Fig. 11a, c), the shortening strain rate is dramatically reduced. Further shortening between minibasins MB1 and MB2 continues at a lower rate by means of MB1 being thrust over MB2.

In the second scenario, in which the diapirs are covered by a roof and the minibasins are thus physically connected, the roof records the resulting strain patterns (Figure 11b). This is especially true between converging MB1 and MB2 (Figure 11d). As the minibasins start translating downslope, the thin minibasins move faster than the intervening thick minibasin. As in the example with no roof, the upslope thin minibasin (MB1) starts to converge with the slower-moving thick minibasin (MB2). In contrast, the downslope thin minibasin (MB3) diverges from the slower-moving upslope minibasin (MB2). The different translation velocities between the minibasins are again accommodated by deformation of the intervening diapirs. However, in this case, the presence of the roof on top of the diapirs results in the development of an additional suite of structures. For example, the roof of diapir D2 stretches and breaks as the thin, faster minibasin MB3 diverges from MB2 (Figure 11b). In contrast, the roof of diapir D1 folds to accommodate the shortening resulting from the upslope, relatively fast, thin minibasin (MB1) converging with the thicker, slower-moving minibasin downslope (MB2) (Figure 11b). The resulting strain and strain rate evolution of the diapirs with roofs is different to the case where the diapirs lack roofs (Figure 12). Much more strain, at higher strain rates, can be accommodated due to the different translation

velocities when the diapirs do not have roofs, and when all the deformation can be cryptically accommodated by the squeezing or stretching of the salt (Figure 12). The evolution of strain and strain rates of intervening diapirs is dependent on the initial slope angle and salt parameters (see also Hamdami et al., 2021). In the case of the diapirs with roofs, strain and strain rate is also strongly dependent on the thickness and mechanical properties of the roof. Here, we have used a relatively weak material to easily allow deformation of the diapir roof. However, if diapir roofs are sufficiently thick or too mechanically strong to accommodate any deformation due to converging or diverging minibasins, the chain of minibasins would likely translate as a single mechanical unit. Different mechanical properties and thickness of the roof would result in different strain and strain rate evolution graphs of the diapirs (see Figure S7).

6 Implications for minibasin kinematics on salt-detached slopes

As salt flows down a slope, minibasins that have developed in the salt layer are also translated. We modelled simple scenarios where the base-of-salt in the slope is smooth. A striking finding from our modelling is that even in the case of a smooth base-of-salt, minibasin translation can still be complex, as minibasins of different thicknesses and geometries can translate at different velocities. Furthermore, minibasin translation can decrease dramatically as the salt beneath them thins ahead of welding (e.g. Krueger, 2010; Wagner and Jackson, 2011). The observations from the numerical models are synthesized in Figures 13a and b, which shows how minibasin thickness, width and density influence minibasin velocity. Minibasins translating at different velocities can converge or diverge, and hence modify strain patterns around them (Figure 11, 12). Shortening is accommodated in between two converging minibasins, while extension occurs in between two diverging minibasins (Figure 13c). This localized shortening and extensional strains can be cryptic if the salt lacks a roof, with minibasin spacing erroneously interpreted as being an original feature.

The base-of-salt in natural salt basins can, however, be highly rugose and have considerable relief (Figure 1c). When minibasins translate downslope over a rugose base-of-salt, if thick enough, the minibasin can weld at its base, or buttress against a high-relief base-salt feature, obstructing the minibasin from further downslope translation (e.g. Krueger, 2010; Wagner and Jackson, 2011; Duffy et al., 2020). The complex deformation patterns that result from different degrees of minibasin obstruction at both the minibasin-scale and the sub-regional scale have been

recently described in detail in an area where the base-of-salt has very high relief (i.e. the northern Gulf of Mexico canopy; Duffy et al., 2020, Fernandez et al., 2020). Minibasin obstruction results in shortening immediately upslope of the obstructed minibasin, and extension on the downslope side of the obstructed minibasin (e.g. Duffy et al., 2020). The interactions between minibasins and the base-of-salt and the potential for minibasins to be obstructed, is important when trying to understand strain patterns around minibasins.

Depending on the initial configuration of minibasins translating at different velocities over a smooth base-of-salt slope, strain patterns can be similar to those described near obstructed minibasins (Duffy et al., 2020), which are generally characterised by up-dip shortening and down-dip extension (Figure 13c). Thus, when attempting to understand strain patterns and minibasin kinematics on salt-detached slopes (see for example Figure 1c), it is important to consider the influence of one, or a combination of: i) minibasin obstruction and interaction with the base-of-salt (*sensu* Duffy et al, 2020); and ii) kinematic interactions between minibasins translating at different velocities in the absence of base-of-salt relief (this study). Assessing whether convergence between minibasins occurred before primary welding and obstruction may be a challenging task if the relative timing of deformation events cannot be constrained. The seismic cross section in Figure 1c, shows an array of minibasins with a thick minibasin that is welded to the base-of-salt in the centre. The diapirs upslope of this welded minibasin have been shortened, as indicated by a secondary weld and folding of the diapir roofs, thus at first glance, the configuration and deformation patterns appear to reflect minibasin obstruction (i.e. shortened diapir immediately upslope of a primary welded minibasin). However, prior to the thick minibasin welding to the base-of-salt, these minibasins were most probably located further upslope from their present position. In fact, the two minibasins upslope of the thicker and presently primary welded minibasin are noticeably thinner. Given this, it is possible that the shortened diapirs are simply the result of differential minibasin translation velocities related to minibasin thickness (as outlined in this study), rather than as a result of primary welding (*sensu* Krueger, 2010; Duffy et al., 2020; Fernandez et al., 2020).

The key finding of this work (that minibasins can translate downslope at different velocities) has been demonstrated in 2D with an analytical solution and numerical models. However, salt flow is three-dimensional. We speculate that in the case of isolated minibasins in 3D, the fundamental principles outlined in this study would still apply, notably in terms of how the minibasin velocity

relates to the overall theoretical salt velocity profile. The isolated minibasins will translate at a slower velocity than the maximum salt velocity (at the salt surface). In 3D, however, increasing minibasin thickness, length (along slope direction) or width (along strike direction), will increase the surface area exposed to viscous drag, more than it would proportionally in 2D.

The implications of considering the three-dimensional behaviour of minibasins extend beyond simple consideration of their velocity, given it may also influence minibasin kinematics and strain patterns. For example, different translation velocities are also possible between neighbouring minibasins that are not necessarily located directly upslope or downslope of one another (i.e. as in our numerical simulations). Where minibasins are slightly offset from the downslope pathway of neighbouring minibasins, additional strike-slip components will be added to the zones of shortening (transpression) and extension (transtension). The complex three-dimensional strains due to differential translation of the sedimentary cover have been previously described using seismic reflection data imaging natural systems (e.g. Krueger, 2010; Duffy et al., 2020; Fernandez et al., 2020), and have also been described from physical models (Dooley et al., 2019; Duffy et al., 2020). In those previous works, strike-slip patterns around minibasins are discussed within the context of minibasins becoming variably obstructed due to welding. However, we emphasise here that different translation velocities between minibasins may be an important contributor to such complex strains, irrespective of any minibasin welding to the base-of-salt.

7 Summary

Due to the viscous behaviour of salt over geologic time and the effect of gravity, a layer of salt lying over an inclined plane flows downslope. Assuming that the thickness of the salt layer is kept constant, the velocity of the flowing salt can be described by a mathematical expression. Such an analytical expression predicts a velocity profile with a maximum salt velocity at the top of the salt layer (salt topography), decreasing to zero at the base of the salt layer. We have reproduced the predictions of the analytical solution for salt flow with 2D numerical simulations of a salt layer overlying an inclined plane.

Returning to our initial question of how fast can minibasins translate on a slope, the answer is that it depends on a number of factors. At a first order approach, the comparison of our numerical simulations with the analytical solution show that minibasins travel at a slower velocity than the

theoretical maximum salt velocity (Figure 9). On top of that, there are a number of factors to consider that will affect minibasin velocity (summarized in Figure 13a).

Minibasin thickness is the main factor controlling minibasin velocity. Thicker minibasins translate slower than thinner minibasins. Furthermore, when the base of the minibasins is close to the base of the salt, the velocity is further decreased. This is true for all minibasins regardless of their density or shape.

In the case of neutral-density minibasins, their thickness remains constant during their translation, and so does their translation velocity. If minibasins are of non-neutral-density, whether they be subsiding or rising, their salt-embedded thicknesses changes during their translation, and so does their velocity. Minibasins that are denser than salt subside into salt as they translate, and if new sediments are deposited, their thickness increases. As the thickness of subsiding minibasins increases, their translation velocity decreases through time. Regardless of the density structure of a minibasin, their velocity can be predicted analytically, as long as they are far enough (minibasin thickness is less than 70% salt thickness) from the base of salt (Eq. (4), Figure 9a,b).

When the minibasin is thick enough so that it is close to the base of salt, minibasin velocity decreases more dramatically than as predicted by Eq. (4) (Figure 9a,b). For such cases, the shape or aspect ratio of the minibasin is another factor to be considered. The aspect ratio of minibasins controls the area or length of the minibasin contact surface at the direction parallel to salt flow exposed to viscous drag. Longer minibasins have more contact surface. The longer the contact surface, the greater the effect of viscous drag at the base of the minibasin is, and therefore, the more the minibasin velocity is reduced (Figure 10).

The findings from our numerical modelling approach have direct and significant implications for understanding minibasin behaviour, kinematics and strain patterns on natural salt-detached slopes. Minibasins of different maturities, and thus differing thicknesses and density structures, can coexist at any given time in the translational domain of a salt-detached continental slope (e.g. Ge et al., 2020). Our study shows that such differences will result in minibasins translating downslope at different velocities. Depending on the initial configuration of the minibasins, this may result in convergence and divergence of minibasins, and minibasins will be able to translate past another in a three-dimensional configuration. These minibasin kinematics will result in deformation being accommodated by the intervening salt structures (e.g. diapirs), or by the overlying sedimentary cover (e.g. diapir roof). When interpreting strain patterns around

minibasins, it is important to consider that shortening and extensional deformation can be the result of minibasins translating at different velocities in continental slopes.

Acknowledgements

MVEP2 numerical code is public and available from https://bitbucket.org/bkaus/mvep2/. The simulations shown in this study were performed with a version of MVEP2 checked from the repository on July 19th 2019, with commit ID number [48165b4]. Color schemes used are from Crameri (2021). Thanks to WesternGeco for providing permission to show the 2D seismic section. The project was funded by the Applied Geodynamics Laboratory (AGL) Industrial Associates program (for an updated list of sponsors check http://www.beg.utexas.edu/agl/sponsors). The authors received additional support from the Jackson School of Geosciences, The University of Texas at Austin.

Appendix A: Derivations of Equations

Supplementary Material

2. References

Aftabi, P., Roustaie, M., Alsop, G.I. and Talbot, C.J., 2010. InSAR mapping and modelling of an active Iranian salt extrusion. *Journal of the Geological Society*, *167*(1), pp.155-170.

Brun, J.P. and Fort, X., 2011. Salt tectonics at passive margins: Geology versus models. Marine and Petroleum Geology, 28(6), pp.1123-1145. Doi: 10.1016/j.marpetgeo.2011.03.004

Brun, J.P. and Fort, X., 2012. Salt tectonics at passive margins: geology versus models–Reply. Marine and Petroleum Geology, 37(1), pp.195-208. Doi: 10.1016/j.marpetgeo.2012.04.008

Brun, J.-P., and Merle, O., 1985, Strain patterns in models of spreading-gliding nappes, Tectonics, 4 (7), 705-719, doi: 10.1029/TC004i007p00705.

Dabrowski, M., Krotkiewski, M. & Schmid, D.W. 2008. MILAMIN: MATLAB based finite element method solver for large problems. Geochemistry, Geophysics, Geosystems, 9, Q04030, Doi: 10.1029/2007GC001719

Cartwright, J., Kirkham, C., Bertoni, Cl., Hodgson, N. and Rodriguez, K., 2018. Direct calibration of salt sheet kinematics during gravity-driven deformation. Geology, 46 (7), pp. 623-626, Doi: 10.1130/G40219.1

Crameri, F., 2021, Scientific colour maps (7.0.1), Zenodo. Doi:10.5281/zenodo.5501399

De Jong, K. A., and Scholten, R. 1973. Gravity and tectonics. New York, John Wiley and Sons, 502 p.

Diegel, F.A., Karlo, J.F., Schuster, D.C., Shoup, R.C. and Tauvers, P.R., 1995. Cenozoic structural evolution and tectono-stratigraphic framework of the northern Gulf Coast continental margin. In. M. P. A. Jackson, D. G. Roberts, & S. Snelson (Eds.), Salt Tectonics: A Global Perspective, AAPG Memoir, Vol. 65, (pp. 109–151). Tulsa, OK: American Association of Petroleum Geologists.

Dooley, T. P., O. B. Duffy, M. Hudec, and N. Fernandez, (2019), Shortening of Diapir Provinces: Translation, Tilting and Rotation of Minibasins in Isolated Minibasin System, *AAPG Annual Convention and Exhibition, San Antonio, Texas*, DOI:10.1306/11229Dooley2019

Duffy, O.B., Fernandez, N., Peel, F.J., Hudec, M.R., Dooley, T.P. and Jackson, C.A.L., 2020. Obstructed minibasins on a salt-detached slope: An example from above the Sigsbee canopy, northern Gulf of Mexico. *Basin Research*, *32*(3), pp.505-524. Doi: 10.1111.bre.12380

Duffy, O.B., Dooley, T.P., Hudec, M.R., Fernandez, N., Jackson, C.A.L., Soto, J.I. 2021. Principles of shortening in salt basins containing isolated minibasins. *Basin Research*, Doi: 10.1111/bre.12550.

Evans, S.L. and Jackson, C.A.L., 2021a. Intra-salt structure and strain partitioning in layered evaporites: implications for drilling through Messinian salt in the eastern Mediterranean. *Petroleum Geoscience*, *27*(4), pp.petgeo2020-072.

Evans, S.L., Jackson, C.A.L. and Oppo, D., 2021b. Taking the pulse of salt-detached gravity gliding in the eastern Mediterranean. *Tectonics*, *40*(7), p.e2020TC006476.

Fernandez, N., Duffy, O.B., Peel, F. and Hudec, M.R., 2021. Influence of minibasin obstruction on canopy dynamics in the northern Gulf of Mexico. *Basin Research*. Doi: 10.1111.bre.12480

Fernandez, N., Hudec, M.R., Jackson, C.A.L., Dooley, T.P. and Duffy, O.B., 2020. The competition for salt and kinematic interactions between minibasins during density-driven subsidence: observations from numerical models. *Petroleum Geoscience*, *26*(1), pp.3-15.

660 Fiduk, J. C., Clippard, M., Power, S., Robertson, V., Rodriguez, L., Ajose, O., Smith, D.
661 (2014). Origin, transportation, and deformation of mesozoic carbonate rafts in the Northern Gulf
662 of Mexico. GCAGS Journal, 3, 20–32.
663 Ge, Z, Gawthorpe, RL, Zijerveld, L, Oluboyo, AP. Spatial and temporal variations in
664 minibasin geometry and evolution in salt tectonic provinces: Lower Congo Basin, offshore
665 Angola. *Basin Res*. 2020; 00: 1– 18. Doi:10.1111/bre.12486
666 Ge, Z., Warsitzka, M., Rosenau, M. and Gawthorpe, R.L., 2019. Progressive tilting of salt-
667 bearing continental margins controls thin-skinned deformation. *Geology*, *47*(12), pp.1122-1126.
668 Ge, Z., Rosenau, M., Warsitzka, M. and Gawthorpe, R.L., 2019. Overprinting translational
669 domains in passive margin salt basins: insights from analogue modelling. *Solid Earth*, *10*(4),
670 pp.1283-1300.
671 Gevantman, L.H. and Lorenz, J., 1981. *Physical properties data for rock salt* (Vol. 167). US
672 Department of Commerce, National Bureau of Standards.
673 Ghassemi, M.R. and Roustaei, M., 2021. Salt extrusion kinematics: insights from existing
674 data, morphology and InSAR modelling of the active emergent Anguru diapir in the Zagros fold
675 and thrust belt, Iran. *Journal of the Geological Society*, *178*(6).
676 Granado, P., Ruh, J.B., Santolaria, P., Strauss, P. and Muñoz, J.A., 2021. Stretching and
677 contraction of extensional basins with pre-rift salt: a numerical modelling approach. *Frontiers in*
678 *Earth Science*, *9*, p.158.
679 Hamdani, I., Aharonov, E., Olive, J.A., Parez, S. and Gvirtzman, Z., 2021. Initiating salt
680 tectonics by tilting: Viscous coupling between a tilted salt layer and overlying brittle sediment.
681 *Journal of Geophysical Research: Solid Earth*, *126*(7), p.e2020JB021503.
682 Jackson, M. P. A., & Hudec, M. R. (2005). Stratigraphic record of translation down ramps in
683 a passive-margin salt detachment. Journal of Structural Geology, 27(5), 889–911. Doi:
684 10.1016/j.jsg.2005.01.010
685 Jackson, M. P. A., & Hudec, M. R. (2017). Salt tectonics: Principles and practice. Cambridge:
686 Cambridge University Press. Doi: 10.1017/97811 39003988
687 Jackson, M. P. A., Hudec, M. R., & Dooley, T. P. (2010). Some emerging concepts in salt
688 tectonics in the deepwater Gulf of Mexico: intrusive plumes, canopy-margin thrusts, minibasin
689 triggers and allochthonous fragments. In Vining, B.A., Pickering, S.C., (eds.) Geological Society,

690 London, Petroleum Geology Conference Series, Petroleum Geology: From Mature Basins to New
691 Frontiers – Proceedings of the 7th Petroleum Geology Conference, 7(1), 899–912.
692 Jackson, M.P.A. and Talbot, C.J., 1991. A glossary of salt tectonics. Geological Circular (Vol.
693 91, No. 4). Bureau of Economic Geology, University of Texas at Austin. Doi: 10.23867/gc9104D
694 Johnson, T.E., Brown, M., Kaus, B.J.P. & VanTongeren, J.A. 2013. Delamination and
695 recycling of Archaean crust caused by gravitational instabilities. Nature Geoscience, 7, 47, Doi:
696 10.1038/ngeo2019
697 Kaus, B.J.P. 2010. Factors that control the angle of shear bands in geodynamic numerical
698 models of brittle deformation. Tectonophysics, 484, 36–47. Doi: 10.1016/j.tecto.2009.08.042
699 Kent, P. E. "Recent studies of south Persian salt plugs." AAPG Bulletin 42.12 (1958): 2951-
700 2972.
701 Krueger, S., (2010). Dynamics of tear faults in the salt-detached systems of the Gulf of Mexico
702 [abs.], in. Proceedings AAPG Annual Convention & Exhibition Abstracts, 19, 137–138.
703 Lees, G.M., 1927. Salzgletscher in Persien. Mitt. geol. Ges. Wien, 22, pp.29-34.
704 Li, S., Abe, S., Urai, J.L., Strozyk, F., Kukla, P.A., Van Gent, H., Berest, P., Ghoreychi, M.,
705 Hadj-Hassen, F. and Tijani, M., 2012. A method to evaluate long-term rheology of Zechstein salt
706 in the Tertiary. *Proc. Mech. Beh. Salt VII*, pp.215-220.
707 Marton, L.G., Tari, G.C., Lehmann, C.T. and Mohriak, W., 2000. Evolution of the Angolan passive
708 margin, West Africa, with emphasis on post-salt structural styles. *Geophysical Monograph-*
709 *American Geophysical Union*, *115*, pp.129-150.
710 Mohammadnia, M., Najafi, M. and Mousavi, Z., 2021. InSAR constraints on the active
711 deformation of salt diapirs in the Kalut basin, Central Iran. *Tectonophysics*, *810*, p.228860.
712 Mukherjee, S., Talbot, C.J. and Koyi, H.A., 2010. Viscosity estimates of salt in the Hormuz
713 and Namakdan salt diapirs, Persian Gulf. *Geological Magazine*, *147* (4), pp.497-507. Doi:
714 10.1017/S001675680999077X
715 Peel, F.J., 2014. The engines of gravity-driven movement on passive margins: Quantifying
716 the relative contribution of spreading vs. gravity sliding mechanisms. Tectonophysics, 633,
717 pp.126-142. Doi: 10.1016/j.tecto.2014.06.023
718 Peel, F. J., Travis, C. J., & Hossack, J. R. (1995). Genetic Structural Provinces and Salt
719 Tectonics of the Cenozoic Offshore U.S. Gulf of Mexico: A Preliminary Analysis. In M. P. A.

720 Jackson, D. G. Roberts, & S. Snelson (Eds.), Salt Tectonics: A Global Perspective, Vol. 65. Tulsa,
721 OK: American Association of Petroleum Geologists. 153- 175. https://doi.org/10.1306/M65604C7
722 Pichel, L.M., Jackson, C.A.L., Peel, F. and Dooley, T.P., 2020. Base-salt relief controls salt-
723 tectonic structural style, São Paulo Plateau, Santos Basin, Brazil. *Basin Research*, *32*(3), pp.453-
724 484.
725 Pichel, L.M., Peel, F., Jackson, C.A. and Huuse, M., 2018. Geometry and kinematics of salt-
726 detached ramp syncline basins. *Journal of Structural Geology*, *115*, pp.208-230.
727 Pilcher, R. S., Murphy, R. T., & McDonough Ciosek, J. (2014). Jurassic raft tectonics in the
728 northeastern Gulf of Mexico. Interpretation, 2(4), SM39–SM55. https://doi.org/10.1190/INT-
729 2014-0058.1
730 Ramberg, H., 1981, Gravity, deformation, and the earth's crust: in theory, experiments, and
731 geological application (2d ed). Academic Press, London; New York. 452p.
732 Rowan, Mark G., Frank J. Peel, and Bruno C. Vendeville. 2004, Gravity-driven fold belts on
733 passive margins, 157-182. In McKley (ed.), Thrust tectonics and Hydrocarbon Systems, AAPG
734 Memoir, Vol. 82. doi: 10.1306/M82813
735 Rowan, M.G., Peel, F.J., Vendeville, B.C. and Gaullier, V., 2012. Salt tectonics at passive
736 margins: Geology versus models–Discussion. Marine and Petroleum Geology, 37(1), pp.184-194.
737 Doi: 10.1016/j.marpetgeo.2012.04.007
738 Schultz-Ela, D.D., 2001, Excursus on gravity gliding and gravity spreading, Journal of
739 Structural Geology, Volume 23, Issue 5, 725-731, doi: 10.1016/S0191-8141(01)00004-9.
740 Schuster, D.C., 1995. Deformation of allochthonous salt and evolution of related salt-
741 structural systems, eastern Louisiana Gulf Coast. In. M. P. A. Jackson, D. G. Roberts, & S. Snelson
742 (Eds.), Salt Tectonics: A Global Perspective, AAPG Memoir, Vol. 65, (pp. 109–151). Tulsa, OK:
743 American Association of Petroleum Geologists.
744 Talbot, C.J. and Rogers, E.A., 1980. Seasonal movements in a salt glacier in
745 Iran. Science, 208(4442), pp.395-397. Doi: 10.1126/science.208.4442.395
746 Talbot, C.J. and Jarvis, R.J., 1984. Age, budget and dynamics of an active salt extrusion in
747 Iran. Journal of Structural Geology, 6(5), pp.521-533. Doi: 10.1016/0191-8141(84)90062-2
748 Talbot, C.J., Medvedev, S., Alavi, M., Shahrivar, H. and Heidari, E., 2000. Salt extrusion at
749 Kuh-e-Jahani, Iran, from June 1994 to November 1997. Geological Society, London, Special
750 Publications, 174(1), pp.93-110. Doi: 10.1144/GSL.SP.1999.174.01.06

751 Tauvers, P.R., 1993. Salt geometry and kinematics, Texas/Louisiana lower slope, northwest
752 Gulf of Mexico Basin. In Salt, sediment and hydrocarbons. Gulf Coast Section Soc. Econ.
753 Paleontol. Min. Foundation 16th Ann. Conf., pp. 271-274. Doi: 10.5724/gcs.95.16.0271.
754 Thielmann, M. & Kaus, B.J.P. 2012. Shear heating induced lithospheric-scale localization:
755 Does it result in subduction? Earth and Planetary Science Letters, 359–360, 1–13, Doi:
756 10.1016/j.epsl.2012.10.002
757 Turcotte, D.L. and Schubert, G., 2002. Geodynamics. Cambridge University Press. New
758 York. 456 p.
759 Urai, J.L., Spiers, C.J., Zwart, H.J. and Lister, G.S., 1986. Weakening of rock salt by water
760 during long-term creep. Nature, 324(6097), pp.554-557. Doi: 10.1038/324554a0
761 Urai, J.L., Schléder, Z., Spiers, C.J. and Kukla, P.A., 2008. Flow and transport properties of
762 salt rocks. *Dynamics of complex intracontinental basins: The central European basin system*,
763 pp.277-290.
764 Wagner III, B.H. and Jackson, M.P., 2011. Viscous flow during salt
765 welding. *Tectonophysics, 510*(3-4), pp.309-326. Doi: 10.1016/j.tecto.2011.07.012
766 Wenkert, D.D., 1979, The flow of salt glaciers. Geophys. Res. Lett., 6: 523-526. doi:
767 10.1029/GL006i006p00523
768 Zhang, S., Jiang, Q., Shi, C., Xu, X., Gong, Y., Xi, J., Liu, W. and Liu, B., 2021. Application
769 of Sentinel-1 and-2 Images in Measuring the Deformation of Kuh-e-Namak (Dashti) Namakier,
770 Iran. *Remote Sensing*, *13*(4), p.785.

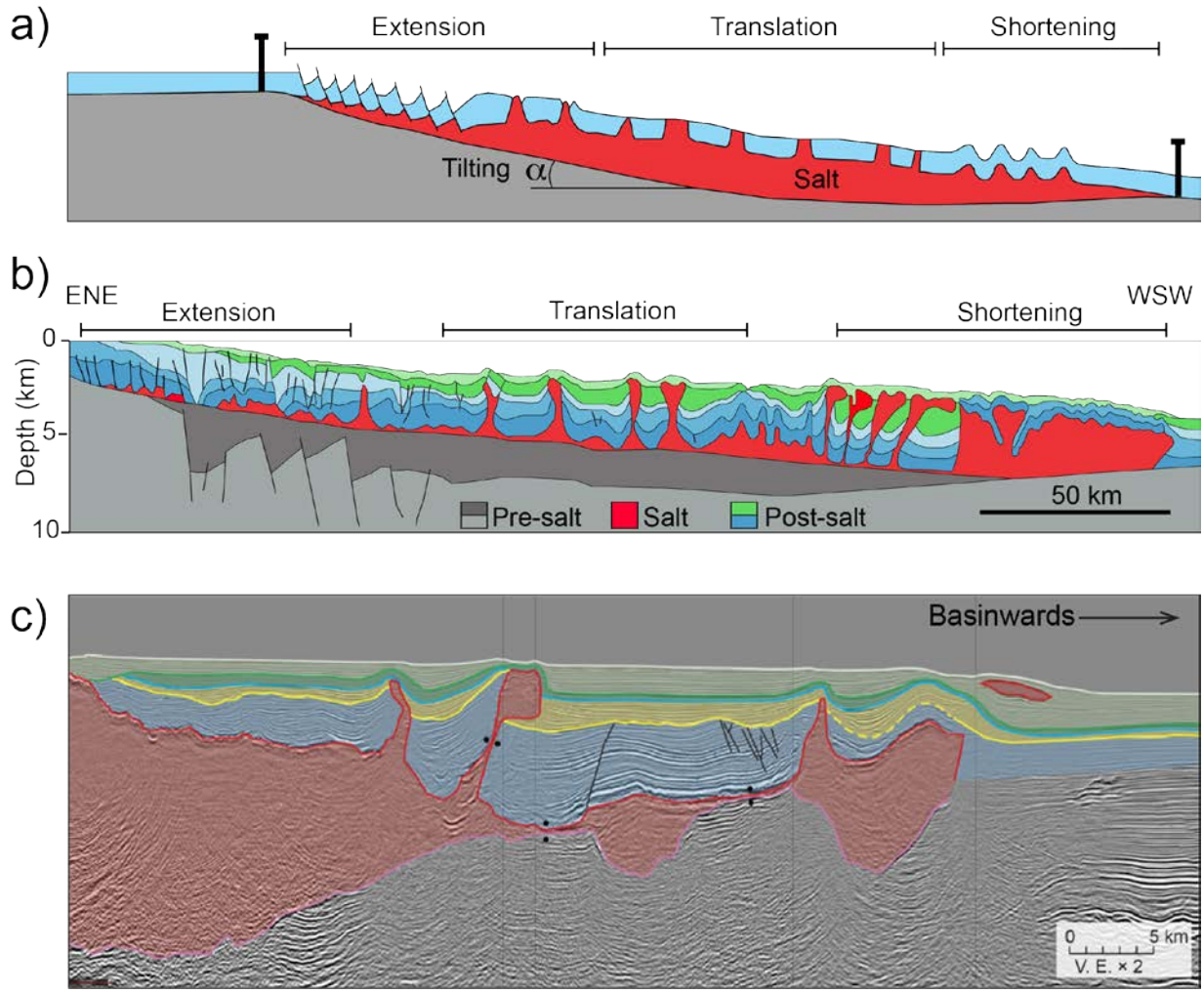

Figure 1. a) Schematic model of a salt-detached slope system with extension-translation-shortening structural zonation. The translational domain is populated with minibasins that translate on top of the salt, as the salt moves downslope. b) Regional interpreted seismic cross section along the Lower Congo Basin (modified from Marton et al., 2000 and Ge et al., 2019) with characteristic downdip shortening domain and updip extension domain. The mid-slope translational zone is characterized by the presence of minibasins and vertical diapirs. c) Seismic cross section of the Northern Gulf of Mexico, where minibasins of different thicknesses can be observed. These minibasins are at present day, close to the lower portion of the slope and the thickest one is welded at the base. However, these minibasin of different thicknesses were initiated and originated at a position further up the slope from their present-day position. Seismic section is shown with permission from WesternGeco.

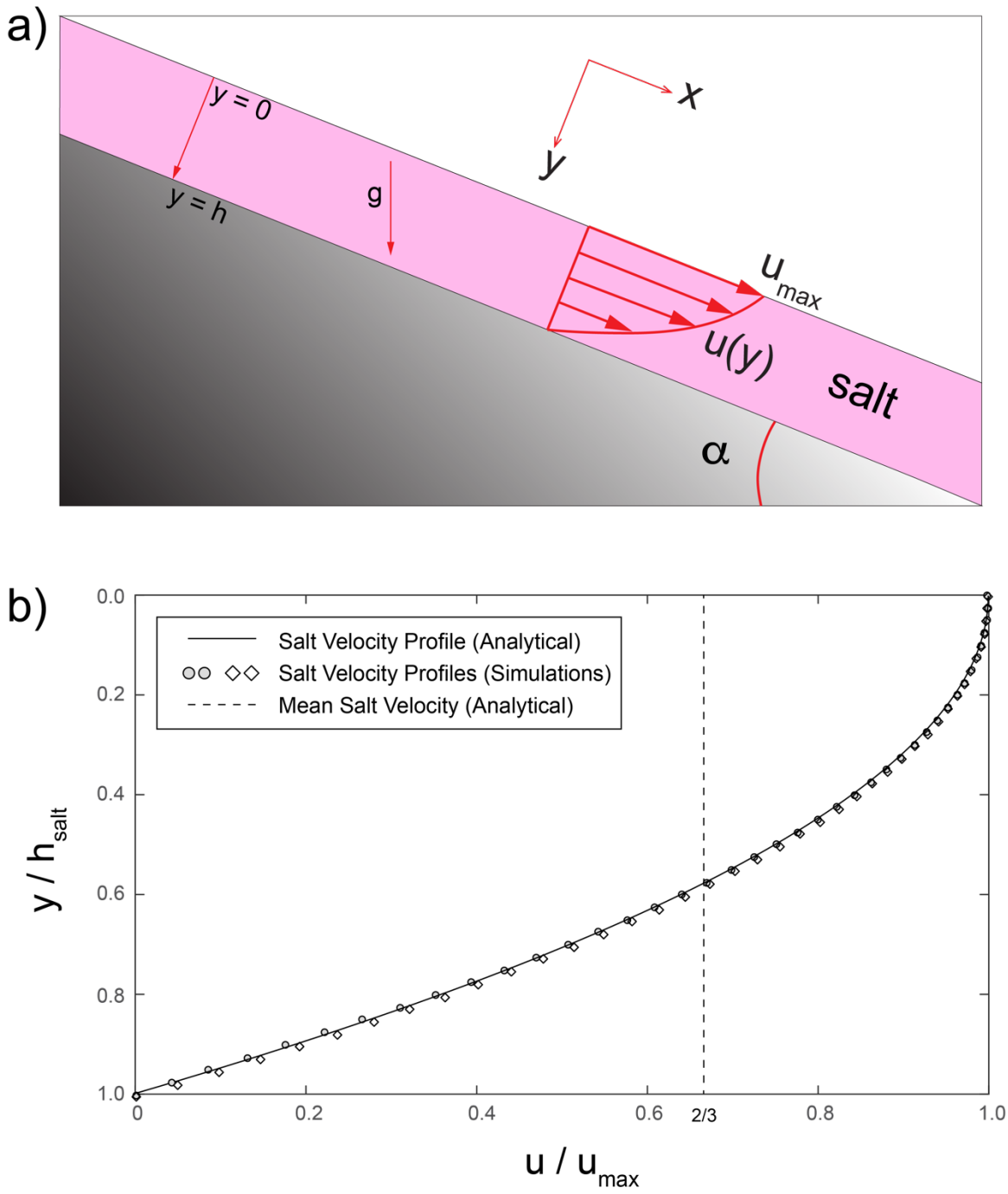

Figure 2. a) Schematic cartoon of a linear viscous salt layer on an inclined plane. The analytical solution assumes that the thickness of the salt layer remains constant. The base of the salt layer has no-slip boundary condition and the top is a free-stress surface. An analytical expression for the resulting velocity (u) profile can be obtained for the given assumptions. See text for details. b) Comparison between the normalized velocity profile calculated from the analytical expression (continuous line) and the velocities extracted from two different numerical simulations (circles and diamonds). The differences between the numerical and analytical solutions are within %1.

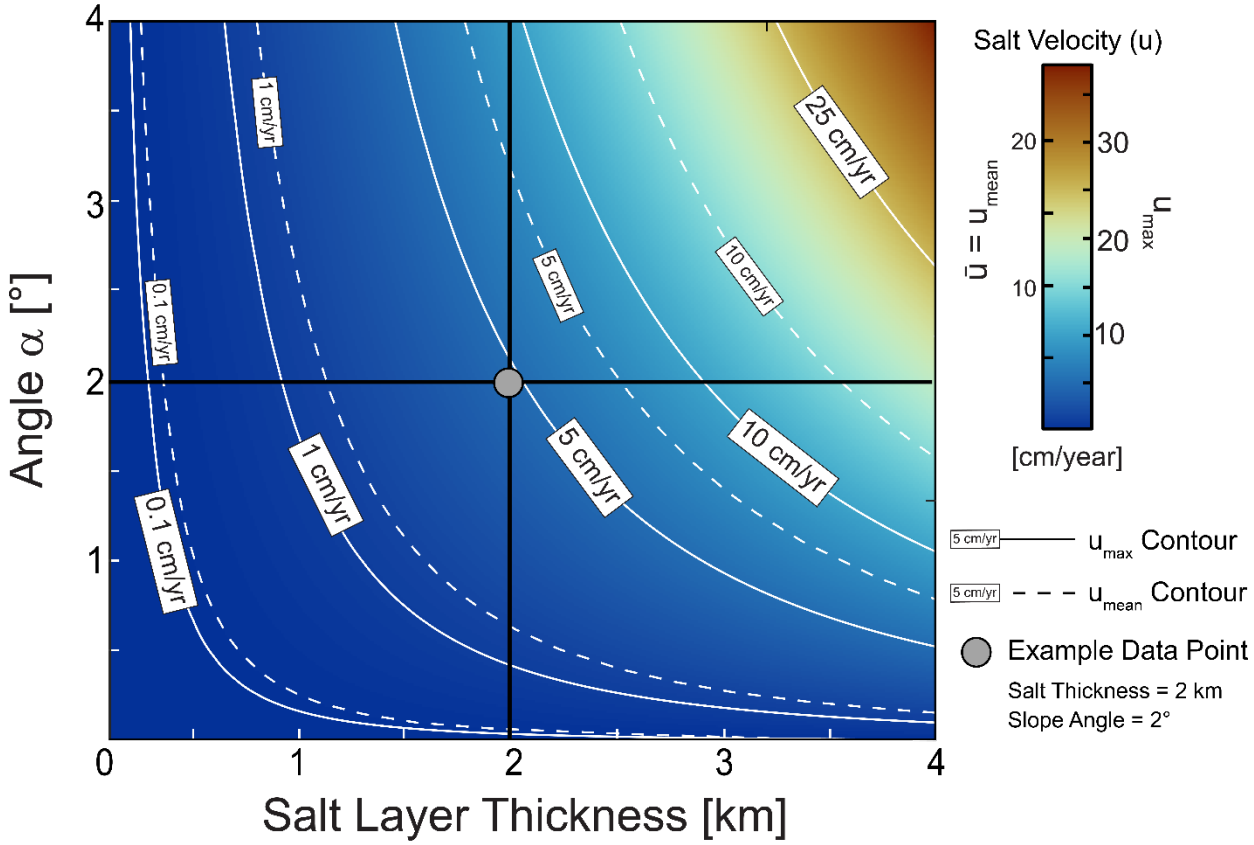

Figure 3. a) Plot of the maximum velocity (u_{max}) and mean velocity (u_{mean}) of the salt layer moving down an inclined plane for a combination of inclination angles and thicknesses of the salt layer. The maximum velocity is obtained at the top of the salt layer. The circle represents the combination of parameters discussed in the text and used in most of the simulations.

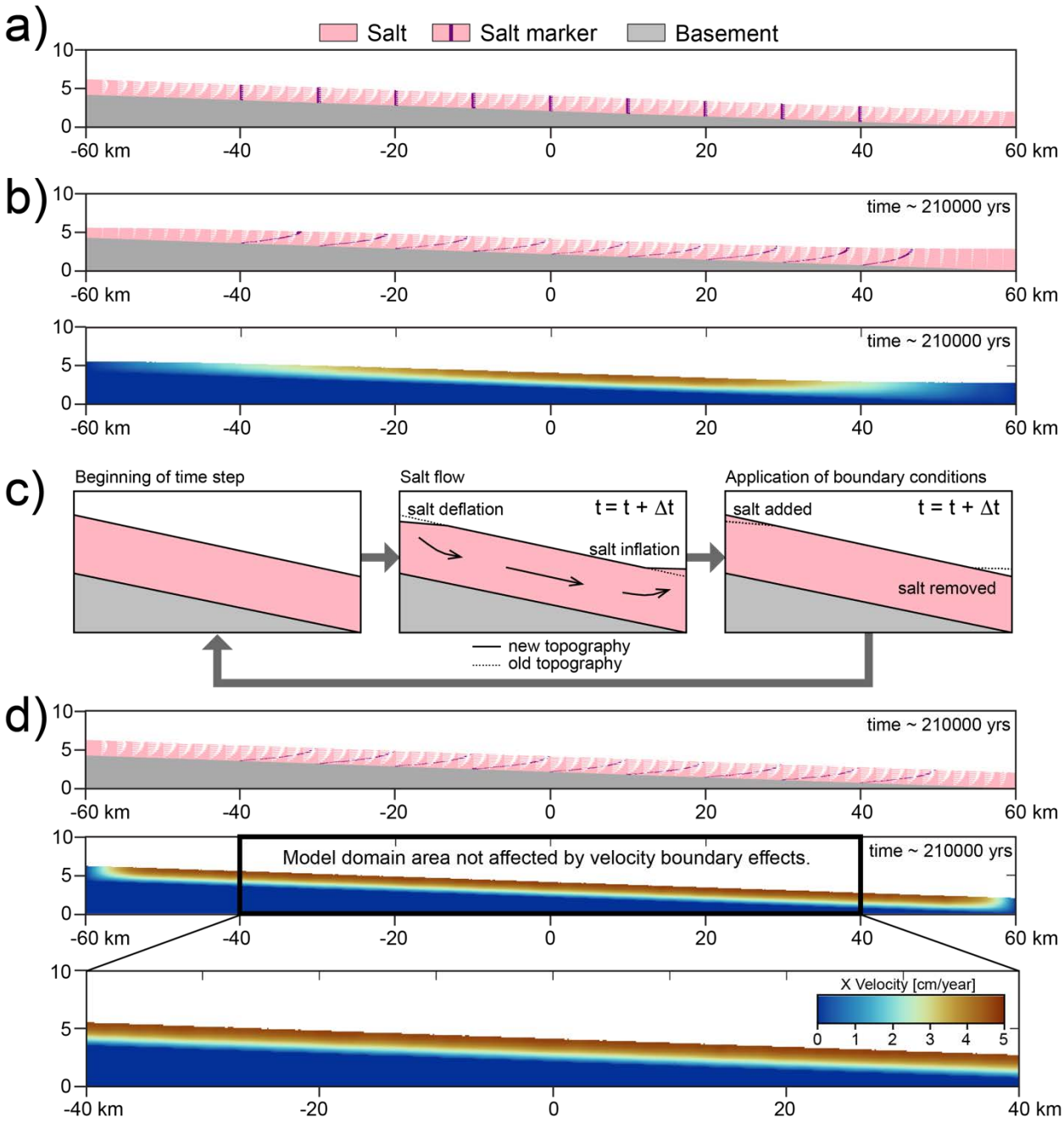

Figure 4. a) Example of an initial model geometry. The modelling box is 120 km x 10 km in size. It contains an inclined basement with a constant thickness layer of salt on top. In this example, the slope angle is α = 2° degrees and salt thickness is H = 2km. b) Intermediate result (geometry in the upper panel and X velocity in the lower panel) of a numerical simulation where the salt is allowed to flow and develop a topography. Starting geometry of the numerical simulation is shown in (a). Note the salt deflation at the updip portion of the slope and the salt inflation at the downdip portion of the slope and the extent of the maximum X velocity area localized in the central portion of the slope. c) Schematic cartoon (not to scale) illustrating the implementation of the internal boundary condition to keep the salt layer thickness constant. The sketched stages are repeated every time step in the numerical simulations. d) Intermediate result of a numerical simulation where the salt thickness is kept constant, by applying an internal boundary conditions as sketched in (c). Note the more homogeneous X velocity profile across the slope compared to (b). The portion of the slope between -40 km and 40 km, is considered to be homogenous and not influenced by edge effects.

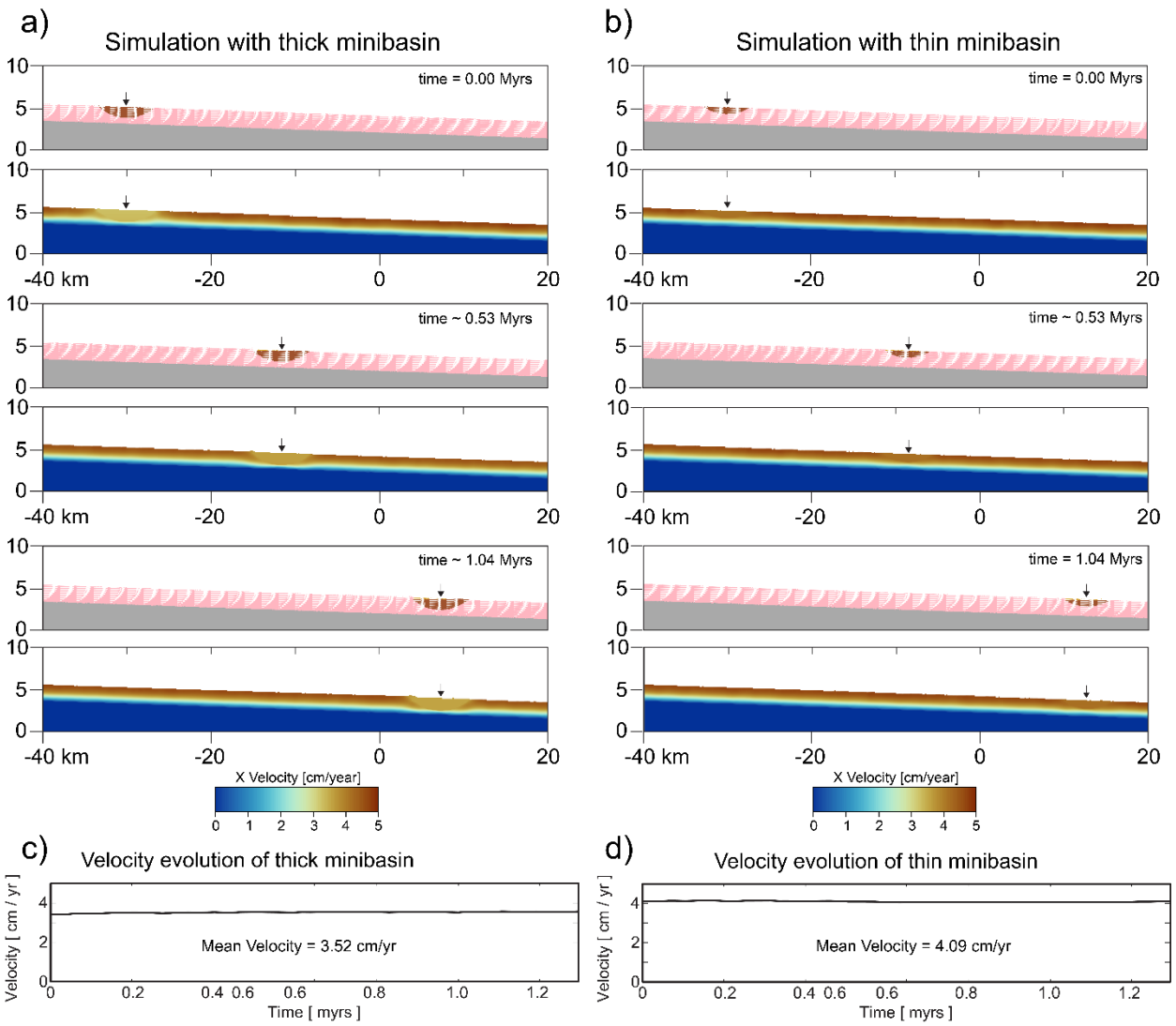

Figure 5. a) and b) Geometry of basement (grey colour), salt (pink colour) and minibasin (brown and orange colours) and velocity field of three different time steps of two numerical simulations. Black arrows indicate the position of minibasins. a) Simulation with a thick minibasin. b) Simulation with thin minibasin. c) and d) Graphs with the evolution through time of the mean velocity of the minibasin from the simulations .c) Simulation with thick minibasin. d) Simulation with thin minibasin. Note that the thin minibasin has higher velocity through time (b and d) and thus, higher mean velocity than the thick minibasin (a and b). The higher velocity of the thin minibasin results in the thin minibasin having advanced further than the thick minibasin in the screenshots shown in (a) and (b).

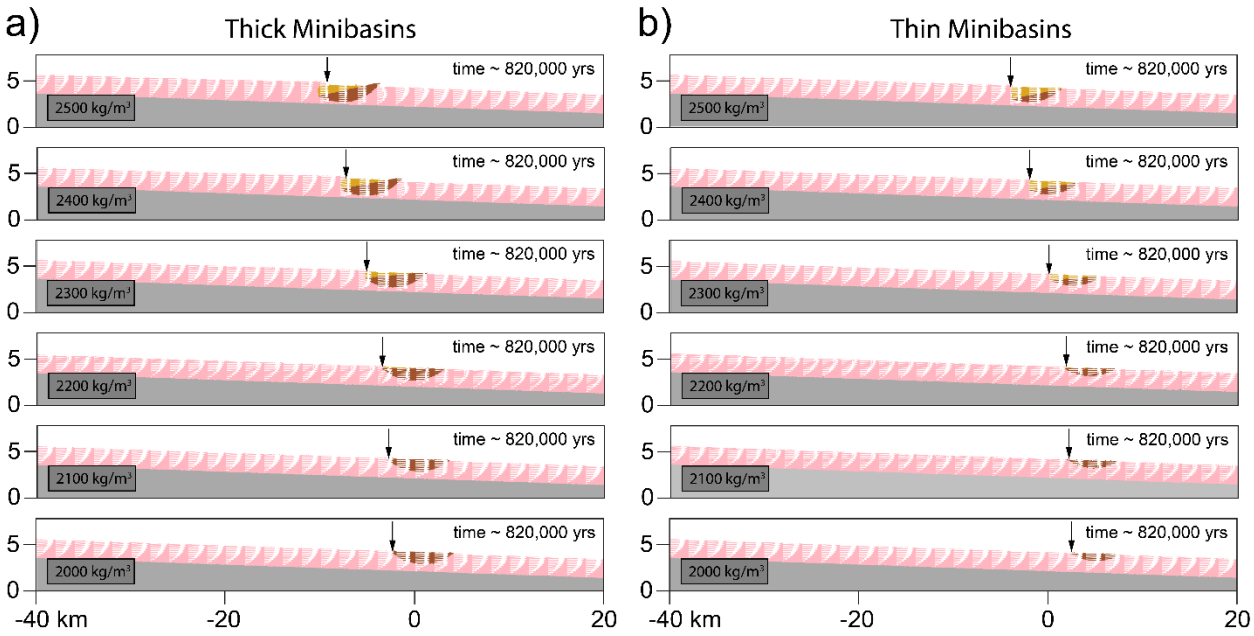

Figure 6. a) and b) Screenshots at the same final time step (time ~820,000 yrs.) of numerical simulations with thick (a) and thin (b) minibasins of different densities. Black arrows indicate the position of the minibasins. The amount of minibasin translation varies according to their densities. Upper panels show the highest density minibasins (denser than salt; 2500, 2400 and 2300 kg/m^3) and have the least amount of translation (a, b). Highest minibasin translation is seen at the lower panel (lowest density minibasin, less dense than salt; 2100 and 2000 kg/m^3). Minibasins that are denser than salt subside as they translate downslope, allowing for sediment accumulation in their up-slope edge, in the form of a synkinematic sediment wedge (orange colour). The accumulation of new sediment results in an increase of minibasin thickness through time.

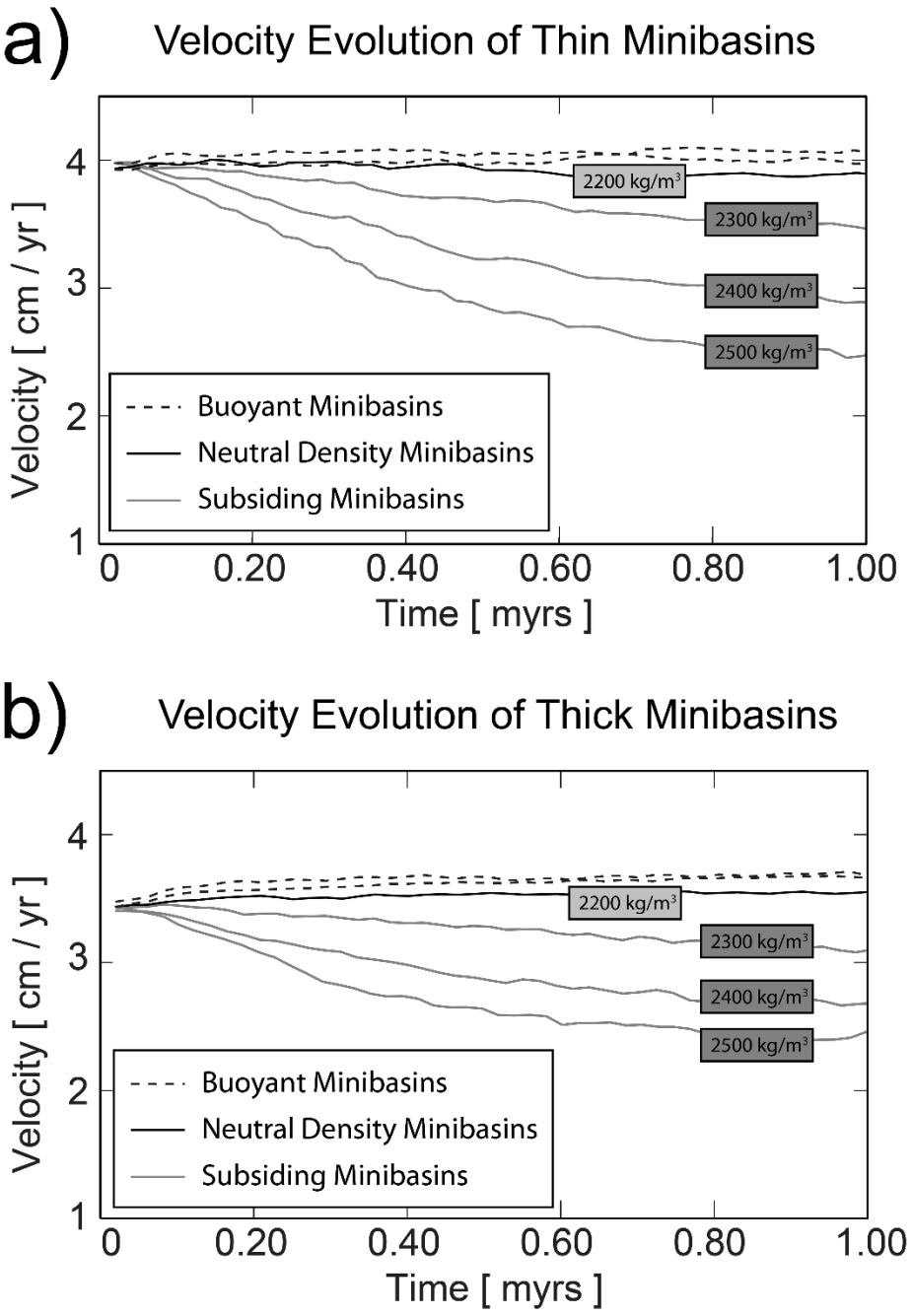

Figure 7. Graphs showing the velocity evolution in simulations with minibasins whose density is different than that of the salt. a) Simulations with thick minibasins. b) Simulations with thin minibasins. Note that, when minibasins are denser than the salt, the velocity of the minibasins tend to decrease through time. Also, the higher the density the faster the decrease in the velocity it is. The opposite is true for minibasins that are less dense than salt, which increase their velocity through time.

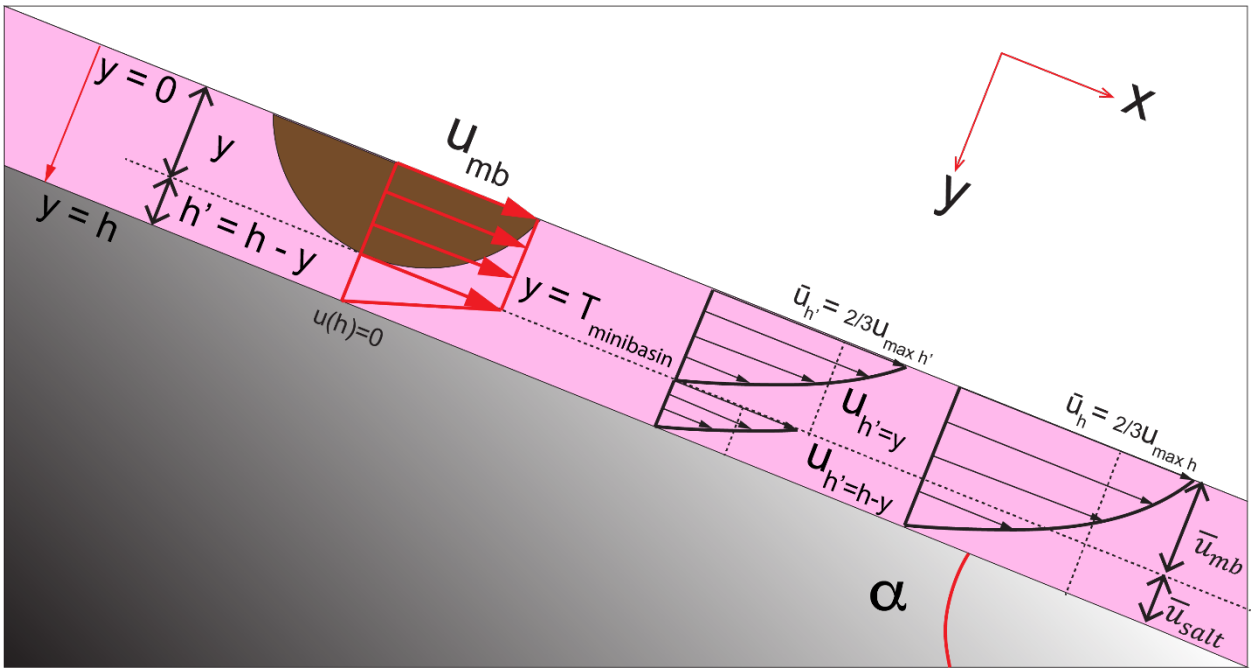

Figure 8. Sketch of a layer of salt on a slope, with a minibasin on it. The position at y that corresponds to the minibasin thickness $y=T_{mb}$ is used to split the salt layer into two portions: upper salt, $h'=y=T_{mb}$ and lower salt, $h'=h-y$. The velocity profile that would correspond to each portion is shown, together with the theoretical salt velocity profile corresponding to the complete salt layer thickness h. The maximum and mean velocities described in the text are illustrated here. $\underline{u}_{mb}$ corresponds to the mean velocity calculated from the upper portion of the velocity profile, that overlaps with the minibasin thickness. $\underline{u}_{salt}$ corresponds to the mean velocity calculated from the lower portion of the velocity profile that is below the minibasin. Both mean velocities can be obtained by integrating the velocity profile for the corresponding portions.

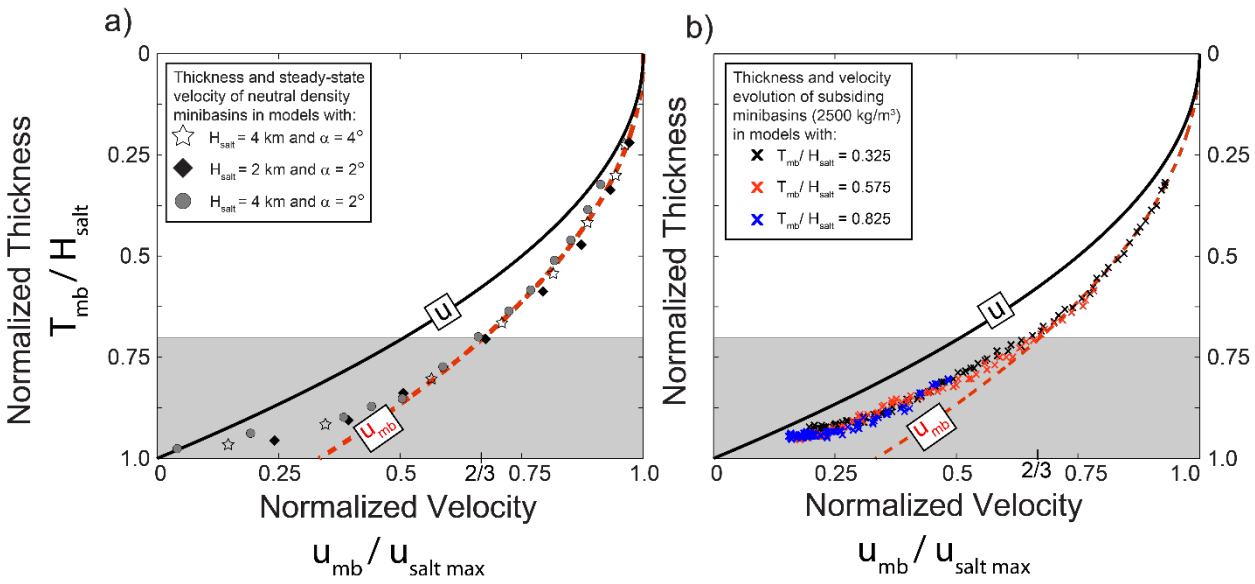

Figure 9. a) Normalized velocity profiles (x axis = u/u_{max}; y axis = y/h) calculated with the analytical solution and equations Eq. 1 (black line), 4 (red line) and 5 (blue line), and the various averaged profiles described in the text (dashed lines). Each of the markers (circles, starts, diamonds) correspond to one numerical simulation with neutral-density minibasins of different initial thickness. Three sets of parameters were used in the numerical simulations of neutral-density minibasins (each set represented by one type of marker, star, circle or diamond). As noted in the text, neutral-density minibasins maintain their translation velocity through time, so for each simulation, the minibasin velocity of a single (initial) time step is plotted in the normalized graph. Overall, the minibasin velocity of the numerical models fall in a curve that relates the salt velocity at the base of the minibasin, and the mean velocity of the portion corresponding to the minibasin thickness (red dashed line). Only, when the initial minibasin thickness is close to the thickness of the salt layer (T_{mb} > 0.7h; greyed area), the velocity is lower than predicted by the curve, and the results plot in a different trend in the graph. b) Normalized velocity profiles (same as in a). Markers (crosses) indicate the minibasin velocity and thickness evolution through time of three simulations in which the minibasin is denser than salt, and thus subsiding. The velocity of subsiding minibasins decreases through time, as they subside and become thicker (see text for details). Overall the velocity and thickness evolution of subsiding minibasins follow a trajectory as described by the analytical curve (red dashed line), until they reach a certain thickness (shaded grey). When the minibasin thickness is closer to the salt thickness (and close to the base-of-salt), the minibasin translation velocity decreases more dramatically.

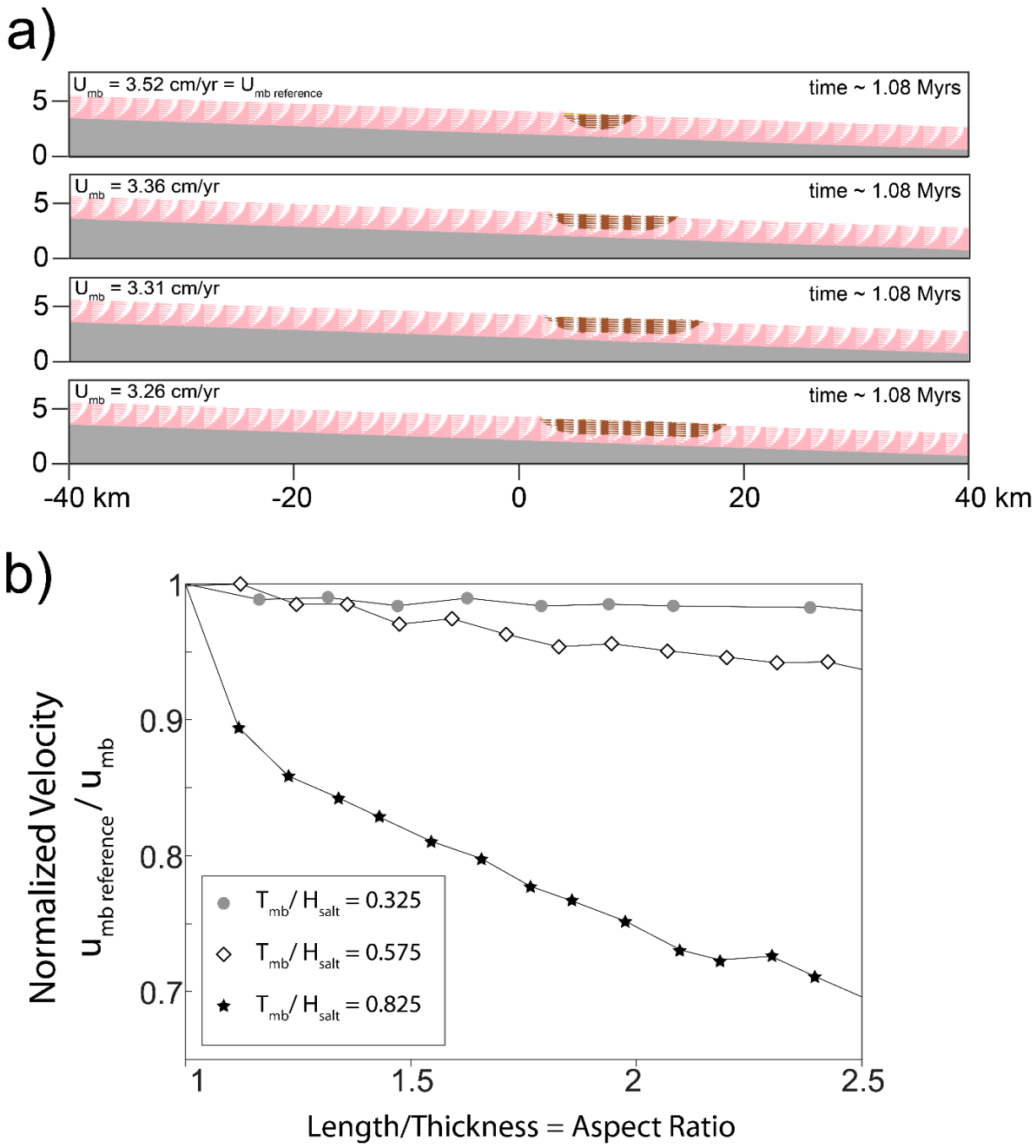

Figure 10. a) Screenshots at the same time-step of four simulations with neutral-density minibasins of same initial thickness but different length or aspect ratio. The minibasin to salt thickness of this example is T_{mb}/H_{salt} = 0.575. The arrow indicates the centre of the minibasin, which at the beginning of the simulations was located at the same position for all cases. The arrow at this time step illustrates that although there has been differential translation, the amount is relatively small. The longest minibasin, which has the highest aspect ratio, (lower panel) has the slowest mean velocity of all, although the differences are relatively small. b) Graph showing the relation between the aspect ratio and minibasin velocity, for neutral buoyancy minibasins with three different initial thicknesses. Each point is one simulation. Each marker type (start, diamond, circle) corresponds to one thickness (e.g. diamond shaped markers correspond to thicknesses shown in (a)). The velocity is normalized to illustrate a decrease from the reference velocity (given by the minibasin with the smallest aspect ratio. Overall, the higher the aspect ratio is, the lower the translation velocity is. However, as discussed in text, thickest minibasins show a higher effect of the aspect ratio.

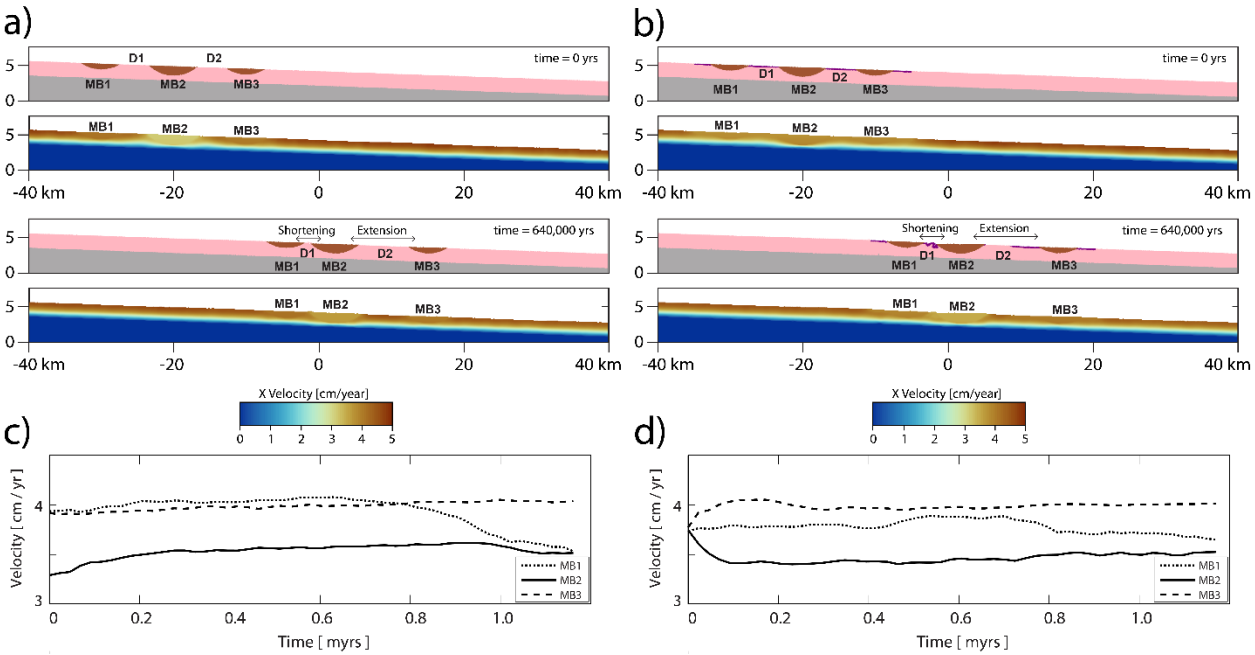

Figure 11. Screenshots of a three time-step evolution of a chain of three neutral-density minibasins on a slope (from updip to downdip, MB1, MB2 and M3; with intervening diapirs D1 and D2). The minibasin in the centre (MB2) is thicker than the ones updip and downdip. Two scenarios are shown. One scenario in which the diapirs are exposed and not covered by a roof (a), and one in which the diapirs are covered by a weak (see text) roof on top (b). The velocities of the minibasins for each scenario are plotted in c) and d). In the simulation with the exposed diapirs (a), as the numerical simulation evolves, the thin minibasins (MB1 and MB3) translate faster than the thick minibasin (MB2) (c). However, as the simulation evolves, updip thin minibasin (MB1), decreases its velocity as it approaches the thick minibasin MB2 (c). In the simulation with covered diapirs (b), because the three minibasins are initially connected by the roof, their starting velocities are the same (d). However, as the simulation evolves, the downdip minibasin (MB3) drifts away from the minibasin in the centre (MB2), the roof in between the two gets stretched (b,d). Instead, the minibasin updip (MB1), converges towards the minibasin in the centre and the roof in between gets shortened by folding (b,c).

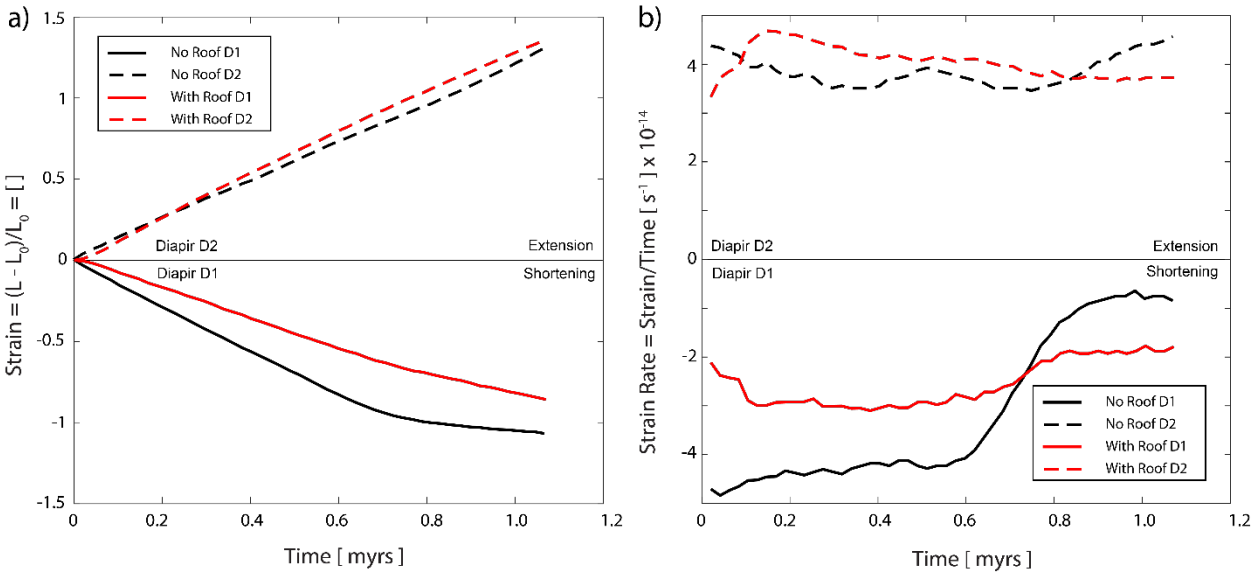

Figure 12. a) Strain accommodated by the diapirs D1 and D2, for the simulations with minibasin arrays and with no roof or with a weak roof. D1 is the diapir located upslope, in between the converging minibasins MB1 and MB2. As such, diapir D1 accommodates the shortening, as shown by the negative value of the strain. The opposite is true for diapir D2, which is located downslope, between diverging minibasins MB2 and MB3. It must also be noted, the higher amount of compressional strain, accommodated by the case in which the diapir has no roof. b) Strain rate calculated for the diapirs D1 and D2. The negative value of the strain rate indicates the shortening which is being accommodated by diapir D1. Note how in the case of the diapir with roof, the initial strain rate of the shortened diapir D1, is less than half than the case of diapir without roof (-2e10^{-14}s^{-1}, compared to -5e10^{-14}s^{-1}). The strain rate of shortened diapir roof is dramatically decreased when minibasins collide (after circa 0.65 Myrs), after which slower shortening can further be accommodated by minibasin overthrusting. Additionally, in the case of the extended diapir D2, both the cases with roof and no-roof start accommodating the deformation early in their evolution.

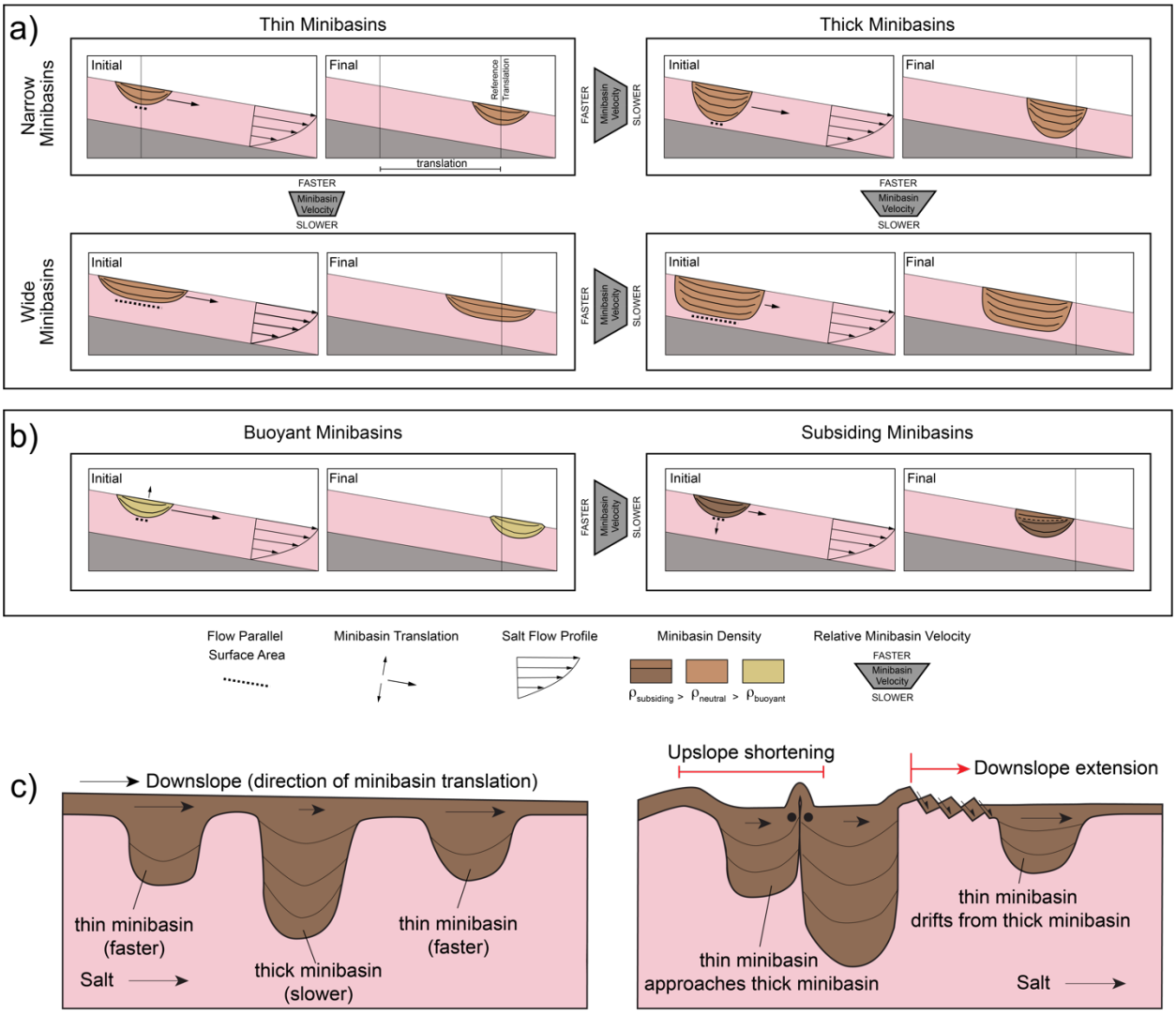

Figure 13. Conceptual sketches reviewing the main controls on minibasin velocity in the numerical simulations with neutral-density minibasins (a) and buoyant and subsiding minibasins (b). a) The main control on minibasin velocity in the case of neutral-density minibasins is the minibasin thickness (or distance to base-of-salt). Thicker minibasins have a lower translation velocity and thus will cover less translation distance for the given time, when compared to thinner minibasins. For a minibasin of a given thickness, its width (measured as an aspect ratio, width to thickness) also influences the translation velocity. A wider minibasin translates slower than a narrow one. The velocity decrease due to higher flow parallel surface area, is even more dramatic in the case of thick minibasins. b) Minibasins that are either buoyant or subsiding will change the distance from the base-of-salt as they translate. Subsiding minibasins create accommodation space for new sediments and increase their thickness, thus reducing their distance from the base of the salt, and ultimately reducing their translation velocity. c) Sketch illustrating that minibasins translating at different velocities can result at similar strain patterns of updip shortening and downdip extension without minibasin obstruction.

Supporting Information

How fast can minibasins translate down a slope?

Observations from 2D numerical models

Naiara Fernandez[1]*, Oliver B. Duffy[1], Christopher A-L. Jackson[2,3], Boris J.P. Kaus[4], Tim Dooley[1], Michael Hudec[1]

[1]*Bureau of Economic Geology, Jackson School of Geosciences, The University of Texas at Austin, University Station, Box X, Austin, Texas, 78713-8924, USA*
[2]*Basins Research Group (BRG), Department of Earth Science & Engineering, Imperial College, Prince Consort Road, London, United Kingdom, SW7 2BP, UK*
[3]*Jacobs, 5 First Street, Manchester, M15 4GU, UK*
[4]*Institute of Geosciences, Johannes Gutenberg University Mainz J.-J.-Becher-Weg 21, D-55128 Mainz, Germany*

**Now at Helmholtz Centre Potsdam GFZ – German Research Centre for Geosciences*
Corresponding author: naiara@gfz-potsdam.de

Supporting Information

We provide the derivation of the analytical solution and supporting figures with definition of the equation terms. We also provide figures of additional numerical simulations that were performed with a salt thickness of 4 km.

Contents of this file

Derivation of Equations

A1. 1D channel flow

Here, we reproduce the steps as described in Turcotte and Schubert (2002) to derive the general expression for the velocity profile, *u(y)* of a viscous fluid in a channel that has the configuration shown in Fig. A1. Where τ indicates shear stress, and p, indicates pressure.

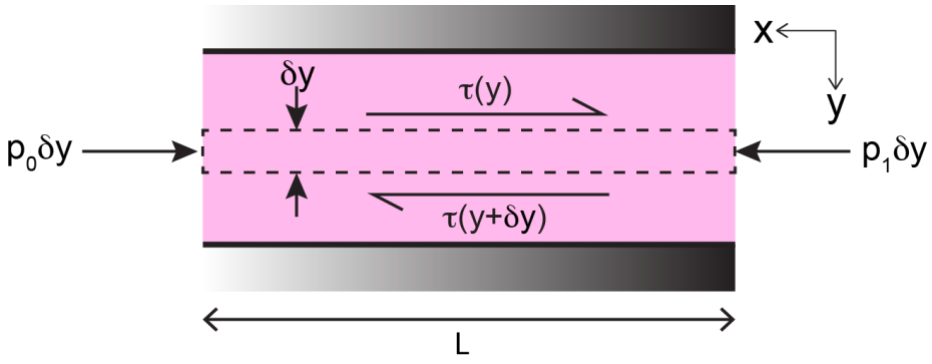

Figure SI-A1. Force balance in a channel with a viscous fluid (in pink) and pressure gradient in the x direction.

In the case of linear viscous fluids (with constant viscosity, μ), the shear stress, τ , at any location of the channel is given by:

$$\frac{du}{dy}\mu = \tau \qquad \text{(A1)}$$

The viscosity of the fluid, μ, is the constant of proportionality between the shear stress, τ, and the strain rate or velocity gradient, $\frac{du}{dy}$.

Flow in channel can be determined by the equation of motion, which implies a force balance on a layer of fluid of thickness δy and length L.

Net pressure force on the element in x direction is $(p_1 - p_0)\,\delta y$, which is the force per unit depth in the direction normal to the plane. For a 1-D channel flow, shear stress and velocity depend only on y.

Shear force on upper boundary of layer is $-\tau(y)L$ and at he lower boundary in x direction is:

$$\tau(y + \delta y)L = \left(\tau(y) + \frac{d\tau}{dy}\,\delta y\right) L \qquad \text{(A2)}$$

The net force in the layer is zero so we can rewrite as follows:

$$(p_1 - p_0)\delta y + \left(\tau(y) + \frac{d\tau}{dy}\,\delta y\right) L - \tau(y)L = 0 \qquad \text{(A3)}$$

$$\frac{d\tau}{dy} = -\frac{(p_1 - p_0)}{L} \qquad \text{(A4)}$$

$$\frac{dp}{dx} = -\frac{(p_1 - p_0)}{L} \qquad \text{(A5)}$$

$$\frac{d\tau}{dy} = \frac{dp}{dx} \qquad \text{(A6)}$$

By substituting $\frac{du}{dy}\mu = \tau$ in Eq. (A6), we obtain:

$$\mu\frac{d^2\tau}{dy^2} = \frac{dp}{dx} \qquad \text{(A7)}$$

Integration of the equation gives,

$$u = \frac{1}{\mu}\frac{dp}{dx}y^2 + C_1 y + C_2 \qquad \text{(A8)}$$

To evaluate the constants, we use the following boundary conditions, of u(h) = 0 and u(0) = u_0, which gives us the following general expression for the velocity in a 1D channel:

$$u = \frac{1}{2\mu}\frac{dp}{dx}(y^2 - hy) - \frac{u_0 y}{h} + u_0 \qquad \text{(A9)}$$

By substituting the Eq. (A9) into the Eq. (A1) of shear stress for viscous flows a general expression for the shear stress in a 1D channel is obtained:

$$\tau = \frac{1}{2}\frac{dp}{dx}(2y - h) - \frac{u_0 \mu}{h} \qquad \text{(A10)}$$

A2. 1D channel flow on an inclined plane

Now, instead of a horizontal channel, let's consider a constant thickness (h) layer of viscous fluid resting on an inclined plane as given in the Fig. A2.

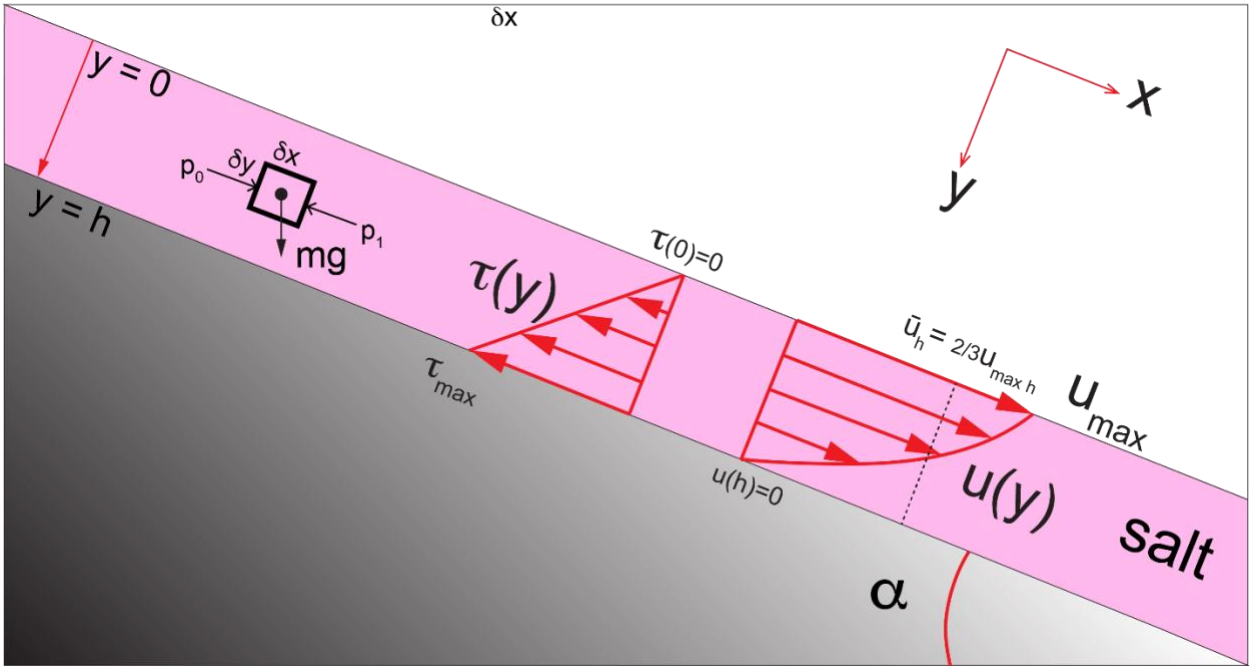

Figure SI-A2. Viscous fluid of constant thickness (in pink) resting on an inclined plane. The force balance in the channel is shown in a small element of dimensions $\delta x, \delta y$. Assuming a free-surface at the top and no-slip at the base of the viscous layer, the resulting velocity and shear stresses are shown.

We will again follow the steps given by Turcotte and Schubert (2002). First, we calculate the pressure gradient in the channel. If we consider a small unit element inside the channel with dimension of δx , δy and in equilibrium, the force in x is given by,

$$F_x = m\ g\ sin\alpha = \delta x\ \delta y\ \rho\ g\ sin\alpha \qquad \text{(A11)}$$

We can then calculate the pressure gradient along the x direction (parallel to the slope) as:

$$p_1 = p_0 + \frac{F_x}{\delta y} \qquad \text{(A12)}$$

$$\delta p = p_0 - p_1 = p_0 - \left(p_0 + \frac{\delta x\ \delta y\ \rho\ g\ sin\alpha}{\delta y}\right) = -\delta x\ \rho\ g\ sin\alpha \qquad \text{(A13)}$$

We can rearrange the equation as:

$$\frac{\delta p}{\delta x} = -\rho\ g\ sin\alpha \qquad \text{(A14)}$$

which is the pressure gradient in x direction due to the slope.

We can substitute the pressure gradient in the previously defined equation of motion in a channel due to pressure gradient (section A1) to obtain:

$$\frac{d\tau}{dy} = -\rho\ g\ sin\alpha \qquad \text{(A15)}$$

By integrating Eq. (A15), we can obtain $\tau(y)$ as:

$$\tau(y) = \int_0^y -\rho\ g\ sin\alpha\ \ dy = -\rho\ g\ sin\alpha\ y + C_1 \qquad \text{(A16)}$$

Assuming free-surface at y = 0, then $\tau(0) = 0$, then $C_1 = 0$.

Which gives a linear shear stress profile, increasing from 0 at the free surface to maximum shear stress at the no-slip base.

As given in Eq. (A1), for linear viscous fluids, we can relate the velocity gradient to the shear stress by the proportionality constant given by the viscosity, which is shown rewritten here:

$$\frac{du}{dy} = \frac{\tau}{\mu} \qquad \text{(A17)}$$

We can use Eq. (A16) and Eq. (17) to obtain the following:

$$u(y) = \int_0^y \frac{\tau}{\mu}\, dy = -\int_0^y \frac{\rho\, g\, sin\alpha\, y}{\mu}\, dy = -\frac{\rho\, g\, sin\alpha\, y^2}{\mu\, 2} + C_2 \qquad \text{(A18)}$$

Assuming no-slip boundary condition at base u(h) = 0, then $C_2 = \frac{\rho\, g\, sin\alpha\, h^2}{\mu\, 2}$. The velocity profile of a constant thickness viscous layer on an inclined plane is given by:

$$u(y) = -\frac{\rho\, g\, sin\alpha\, y^2}{\mu\, 2} + \frac{\rho\, g\, sin\alpha\, h^2}{\mu\, 2} = \frac{\rho\, g\, sin\alpha}{\mu\, 2}\,(h^2 - y^2) \qquad \text{(A19) or } \mathbf{Eq.\ (1)}$$

The velocity profile that results from a constant thickness layer with a free surface at the top, is not linear, but parabolic (as seen in the picture).

The maximum velocity at this case, occurs at the free-surface (y=0) where the shear stress is zero.

$$u_{\max\ h} = u(0) = \frac{\rho\, g\, sin\alpha\, h^2}{\mu\, 2} \qquad \text{(A20) or } \mathbf{Eq.\ (2)}$$

And the mean velocity can be obtained by integrating the velocity profile for the layer thickness and dividing it by the thickness.

$$u_{mean\,h} = \bar{u}_h = \frac{1}{h}\int_0^y u(y)\,dy = \frac{\rho\, g\, sin\alpha\, h^2}{\mu\, 3} = \frac{2}{3}u_{\max\, h} \qquad \text{(A21) or } \mathbf{Eq.\ (3)}$$

Equations (1), (2) and (3) are the ones used in the main text.

A3. Velocity profiles for (sub-)layers defined within an inclined viscous layer

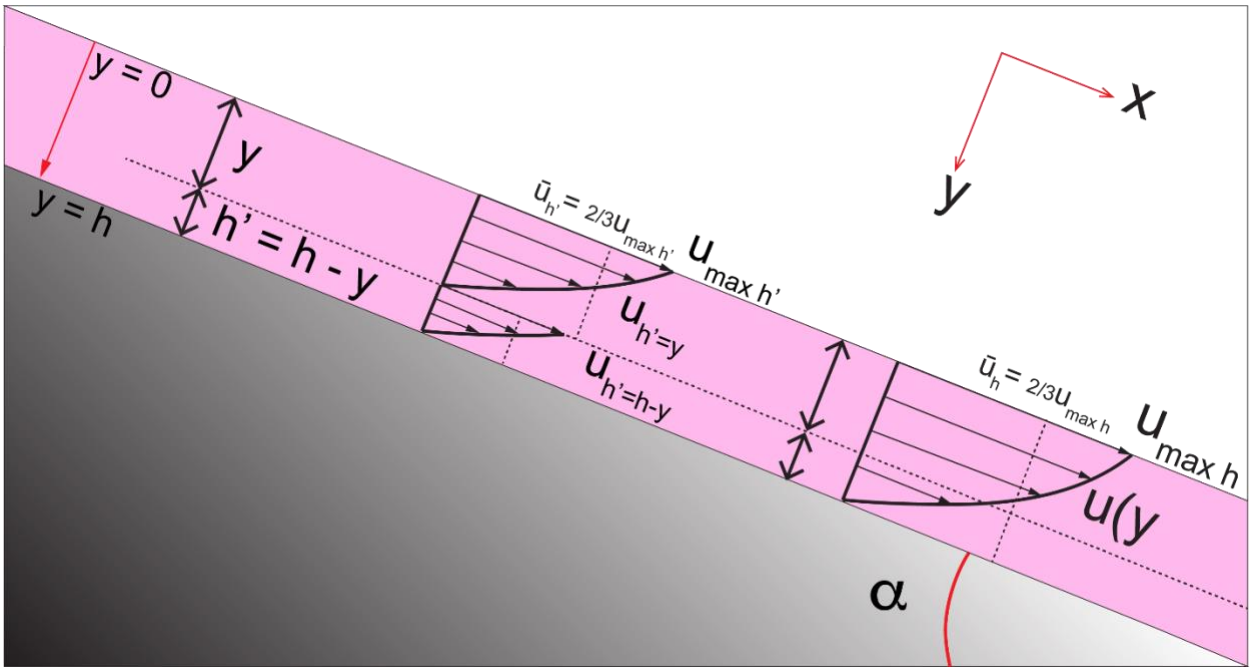

Figure SI-A3. Schematic illustration of the resulting velocity profiles when instead of the total thickness (h) of the viscous layer, partial thicknesses are considered. Upper portion where h'=y and lower portion where h'=h-y.

Now, instead of considering one unique velocity profile for the layer thickness of h of the entire viscous layer, we will consider the velocity profiles for (sub-)layers whose thicknesses, h', range between 0 and y (h'=y) and between y and h (h'=h-y) (see Fig. A3). In the case of h' = y, the maximum and mean velocities of the viscous (sub-)layers with thicknesses between 0 and y, can be calculated as:

$$u_{\max\, h'=y} = \frac{\rho\, g\, sin\alpha\, (y)^2}{\mu\, 2} \qquad \text{(A22)}$$

$$u_{\text{mean } h'} = \bar{u}_{h'=y} = \frac{\rho\, g\, sin\alpha\, (y)^2}{\mu\, 3} \qquad \text{(A23)}$$

Subtracting $u_{\max at\ y}$ from $u_{\max for\ h}$ gives the $u(y)$ of Eq. (A19) or Eq. (1):

$$u_{\max\ h} - u_{\max\ h'=y} = u(y) \qquad \text{(A24)}$$

Additionally, we consider the case of layers whose thicknesses h', range between y and h (h'=h-y). In this case, instead of having a unique value for the maximum and mean velocities, we have a range of values as given by:

$$u_{\max\ h'=h-y} = \frac{\rho\, g\, sin\alpha\, (h\prime)^2}{\mu\, 2} = \frac{\rho\, g\, sin\alpha\, (h-y)^2}{\mu\, 2} \qquad \text{(A25)}$$

$$\bar{u}_{h'=h-y} = \frac{\rho\, g\, sin\alpha\, (h')^2}{\mu\, 3} = \frac{\rho\, g\, sin\alpha\, (h-y)^2}{\mu\, 3} \qquad \text{(A26)}$$

A4. Minibasin on an inclined viscous layer

All the calculations in the previous sections consider the 1D flow channel equations. However, in the numerical models presented in the main text, minibasins are present in the slope. We will consider the minibasin being of the same density as the fluid, but a much higher viscosity (10^{25} Pa s). The viscosity of the minibasins is so high compared to the surrounding viscous fluid, that it effectively behaves as a rigid body, and it will translate down slope with a homogeneous velocity. These minibasins have a finite lateral extend, so there is a variation of velocity and shear stress along the x direction, which is not considered in the 1D channel flow equations. Despite this along X variation in velocity and shear stress, we can try to relate the minibasin velocity obtained from the models with the equations of 1D channel flows.

As in the previous section, we consider the viscous layer as divided in two portions from 0 to y and from y to h, but now we consider that y corresponds to the minibasin thickness, T_{mb}. See Fig. A4. The salt layer is then divided between 0 and $y=T_{mb}$ and between $y=T_{mb}$ and h. We will refer to these portions of the minibasin layer as upper portion and lower salt layer portion.

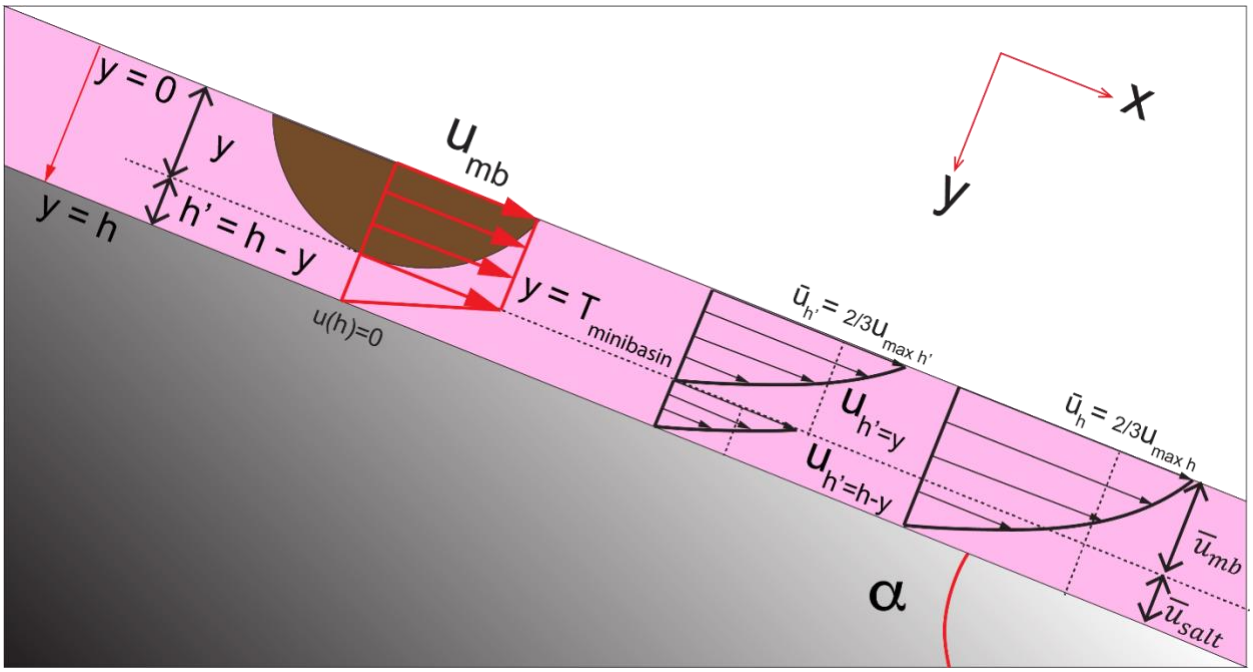

Figure SI-A4. Schematic illustration of the viscous layer (in pink) resting on an inclined plane. A minibasin (in brown) of density equal to that of the viscous fluid with a circular geometry is present in the viscous fluid. The thickness of the minibasin is T_{mb}.

The minibasins of the numerical simulations shown in this work, are sub-circular in shape, as illustrated in Fig. A4. However, we can also consider, rectangular shape minibasins with vertical walls and flat base as shown in Fig. A5.

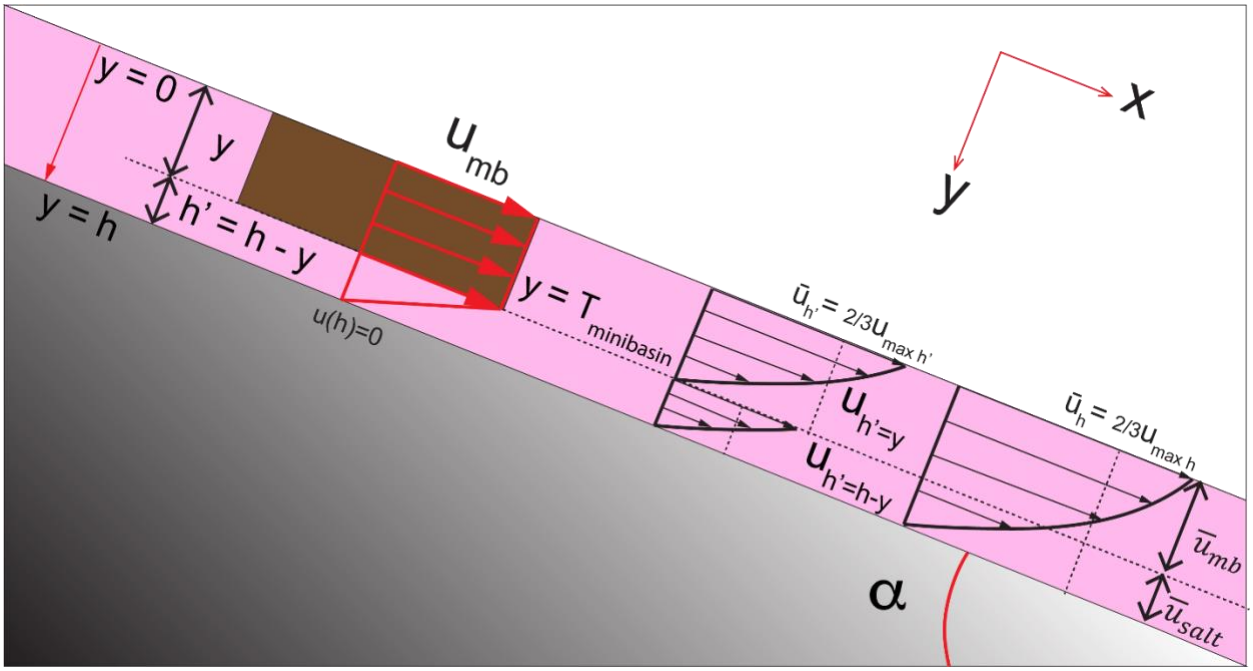

Figure SI-A5. Schematic illustration of the viscous layer (in pink) resting on an inclined plane. A minibasin (in brown) of density equal to that of the viscous fluid with a rectangular geometry is present in the viscous fluid. The thickness of the minibasin is T_{mb}.

Let's first consider the salt velocity profile calculated for the full thickness of the salt (h) and calculate the mean velocity of salt layer corresponding to the portions covering the minibasin thickness (upper portion) and the thickness below the minibasin (lower portion). We will call these velocities $\bar{u}_{mb}$ and $\bar{u}_{salt}$ respectively.

$$\bar{u}_{mb} = \frac{1}{y}\int_0^y u\,\partial y = \frac{1}{y}\frac{\rho\, g\, sin\alpha}{2\mu}\left(h^2 y - \frac{y^3}{3}\right) \qquad \text{(A27)}$$

$$\bar{u}_{salt} = \frac{1}{h-y}\int_{h-y}^{h} u\,\partial y = \frac{1}{h-y}\frac{\rho\, g\, sin\alpha}{2\mu}\left(\frac{2h^3}{3} - h^2 y - \frac{y^3}{3}\right) \qquad \text{(A28)}$$

Similarly, we can consider the equations from the previous section, where we calculated the maximum and mean velocity for viscous layers of thickness between 0 and h'=y, but now we consider y = T_{mb}.

$$u_{\max\ y=Tmb} = \frac{\rho\ g\ sin\alpha\ (y)^2}{\mu\ 2} \qquad \text{(A29)}$$

$$\bar{u}_{y=Tmb} = \frac{\rho\ g\ sin\alpha\ (y)^2}{\mu\ 3} \qquad \text{(A30)}$$

The equations for 1D channel flows are plotted in a normalized graph. The x-axis represents the velocities, normalized over the maximum velocity for a free-surface. T y-axis represents the thickness of a sub-portion of the total layer of thickness, normalized over the total thickness of the layer (h).

The results from the numerical simulations with minibasins can be plotted on the graph with the theoretical equations (minibasin velocity and thickness). Similarly, results of numerical models of rafts or sediment blocks (vertical walls, instead of circular walls) are plotted.

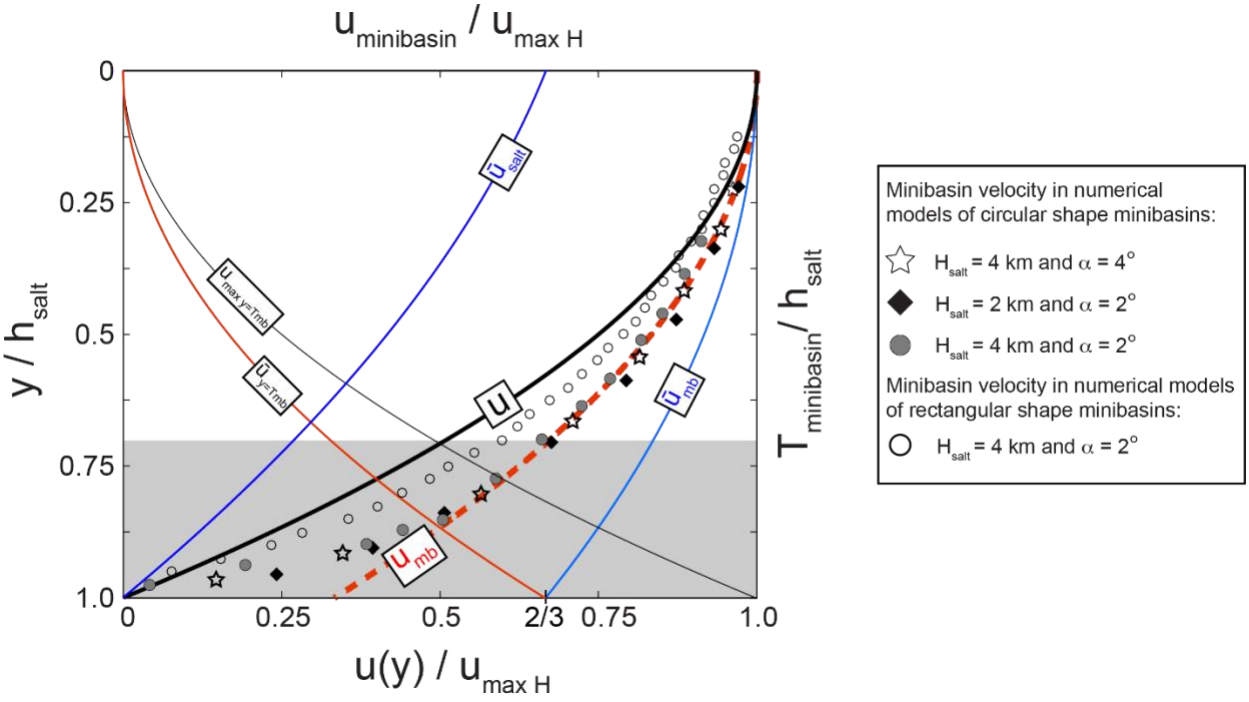

Figure SI-A4. Normalized plot with the solid-line graphs corresponding to the 1D channel flow derived equations as described in the text. Markers correspond to results of 2D numerical simulations with rectangular minibasins (hollow circles) and circular minibasins (grey circles, black diamonds, hollow starts) for the simulation parameters shown in the legend.

The numerical models show that thin minibasins translate faster than thick minibasins. The relation between thickness and minibasin velocity in the case of minibasins of circular shape describes a curve in the graph. In fact, the results from the numerical simulations with minibasins plot on top of a curve that can be described by the following equation,

$$u_{mb} = u_{\max\ h} - \bar{u}_{y=Tmb} = \frac{\bar{u}_{mb}+u(y)}{2} = \frac{\rho\ g\ sin\alpha\ h^2}{\mu\ 2} - \frac{\rho\ g\ sin\alpha\ y^2}{\mu\ 3} \quad \text{(A31) or } \mathbf{Eq.\ (4)}$$

Eq. (4) is used in the main text to predict the velocity of sub-circular minibasins in the numerical simulations.

However, the minibasins with a rectangular shape (vertical walls), plot closer to the graph described by $u(y)$. In addition, Increasing the length (width) of the minibasin, but keeping their thickness the same, reduces minibasin velocity, moving the velocity value in the graph to the left. The lower limit for the velocity of a minibasin of given thickness is the velocity described by u(y). The velocities calculated in numerical simulations with minibasins of different geometries (aspect ratios, sub-circular or rectangular), plot in the area of the graph between $u(y)$ and u_{mb}.

Thus, although the equations are derived for 1D channel flows, they can be used to predict the velocity of sub-circular minibasins as shown in the main text.

References

Turcotte, D.L. and Schubert, G., 2002. Geodynamics. Cambridge University Press. New York. 456 p.

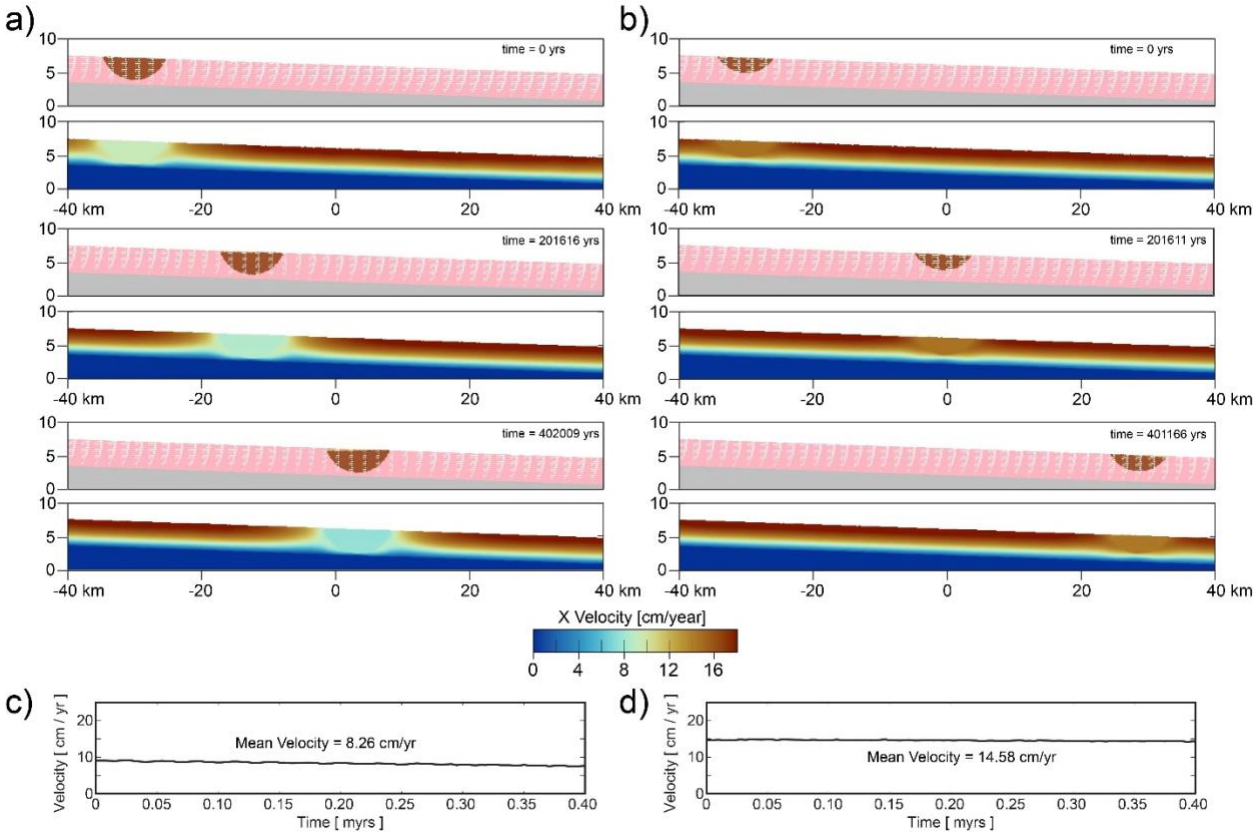

Figure SI-5. a) and b) Screenshots with plots of composition and velocity field of three different time steps of two numerical simulations of salt moving downslope. a) Simulation with thick minibasin b) Simulation with thin minibasin. c) and d) Graphs with the evolution through time of the mean velocity of the minibasin from the two simulations. c) Simulation with thick minibasin. d) Simulation with thin minibasin. Note that the thin minibasin has higher velocity through time (c) and thus, higher mean velocity than the thick minibasin (d). The higher velocity of the thin minibasin results in the thin minibasin having advanced further than the thick minibasin in the screenshots shown in (a) and (b).

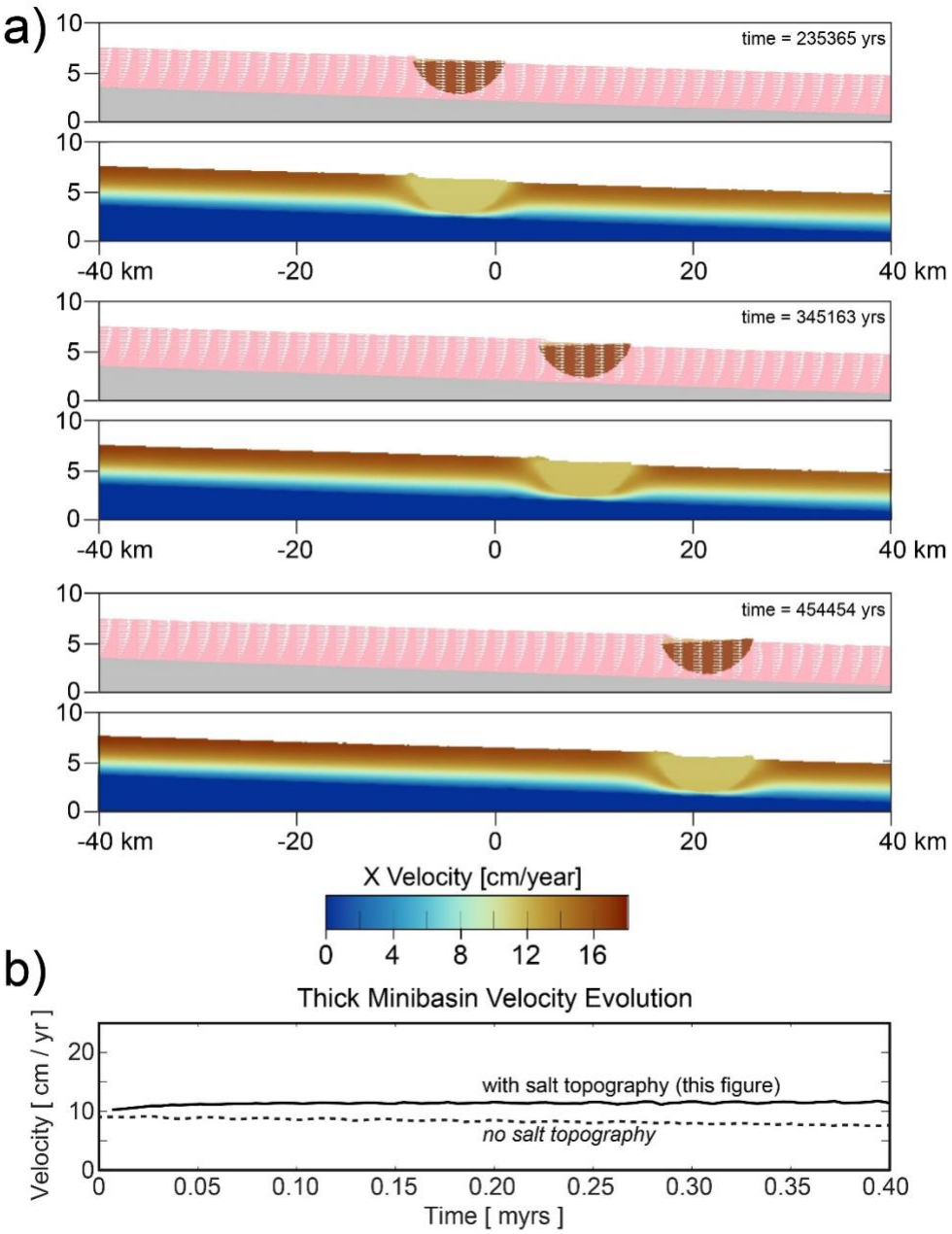

Figure SI-6. a) Screenshots of four time-step evolution of a numerical simulation with a thick minibasin. In this simulation, implemented boundary conditions, allowed for the development of salt topography. As a result, shallow, faster moving salt is extruded on top of the slow moving minibasin during the translation. b) Graph showing the velocity evolution of the minibasin in the simulation with salt topography (continuous black line, simulation shown in this Figure), and of the minibasin in the simulation with no-salt topography allowed (dashed black line, simulation shown in previous Figure). Note that in the simulation where salt-topography could develop the minibasin velocity increased with time. In this particular case where, the average velocity of the thick minibasin is dramatically slower than velocity of the shallow (i.e. upper) portion of the salt, and the faster-flowing salt up-dip of the minibasin extrudes onto the minibasin. The load of the salt extrusion on top of the minibasin enhances the tilt of the minibasin and the overall effect of the process is a slight increase of the minibasin velocity through time.

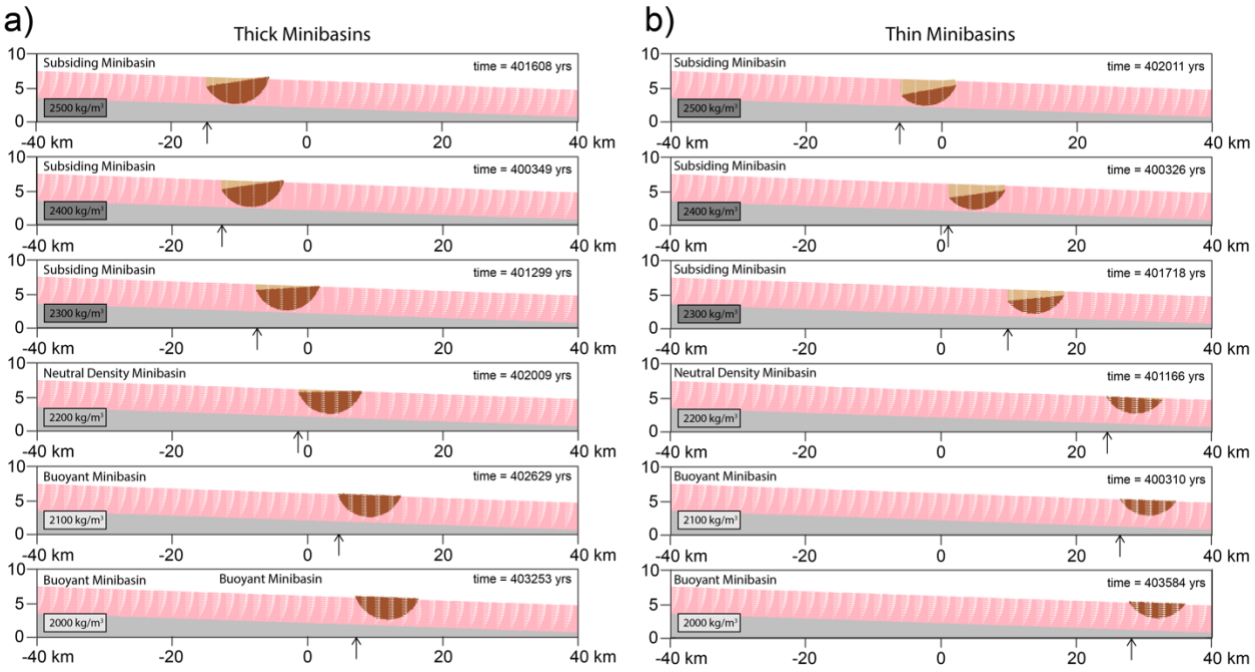

Figure SI-7. a) and b) Screenshots at the same final time step (time =~400000 yrs.) of numerical simulations with thick (a) and thin (b) minibasins of different densities. The amount of minibasin translation varies according to their densities. Upper panels show the highest density minibasins (denser than salt) and have the least amount of translation (a, b). For simulations with different minibasin densities, final minibasin translation is higher (a, b). Highest minibasin translation is seen at the lower panel (lowest density minibasin, less dense than salt). Minibasins that are denser than salt subside as they translate downslope, allowing for sediment accumulation in their up-slope edge. The accumulation of new sediment results in an increase of minibasin thickness trough time.

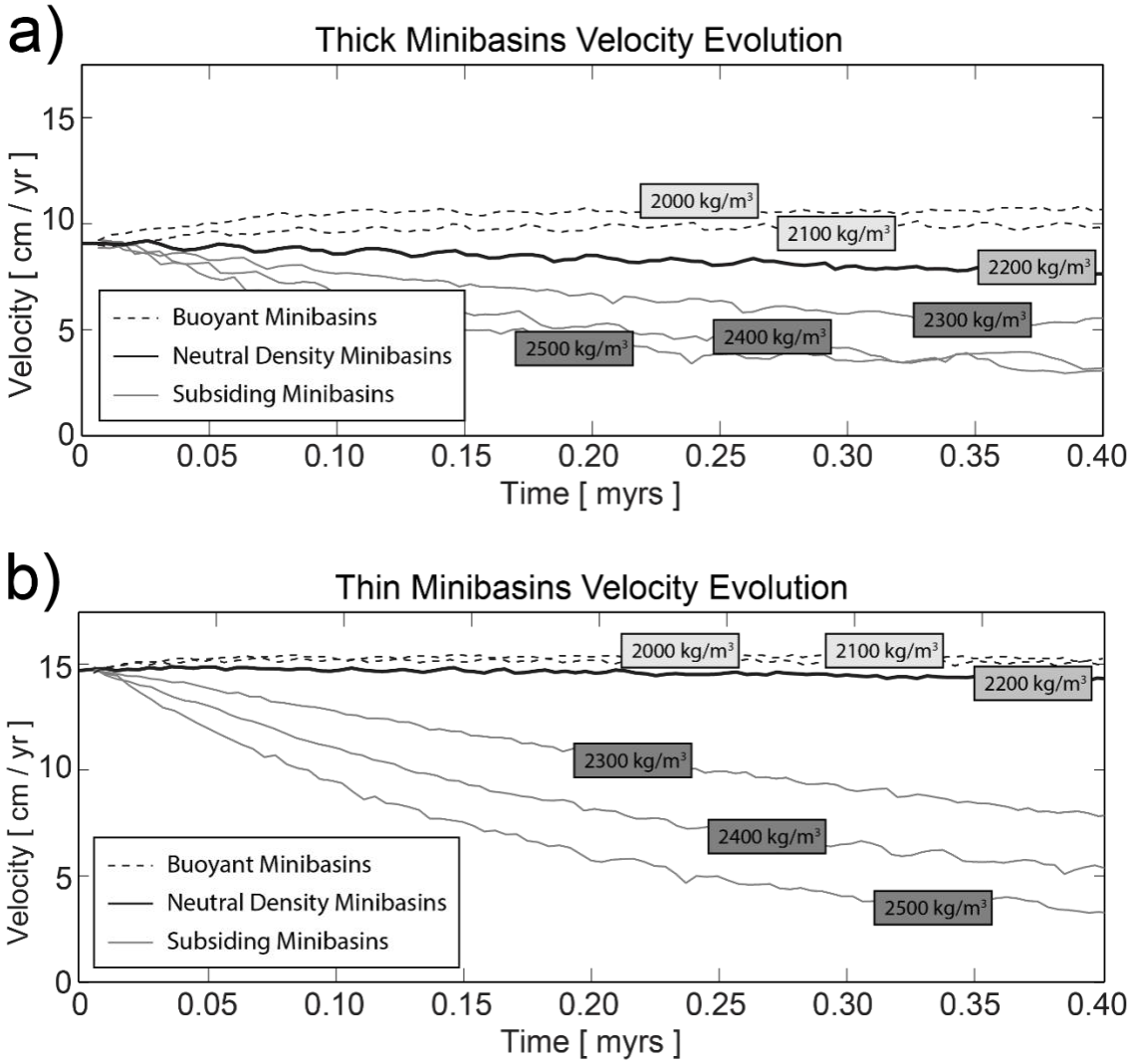

Figure SI-8. Graphs showing the velocity evolution in simulations with minibasins whose density is different than that of the salt. a) Simulations with thick minibasins. b) Simulations with thin minibasins. Note that, when minibasins are denser than the salt, the velocity of the minibasins tend to decrease through time. Also, the higher the density the faster the decrease in the velocity it is. The opposite is true for minibasins that are less dense than salt, which increase their velocity through time.

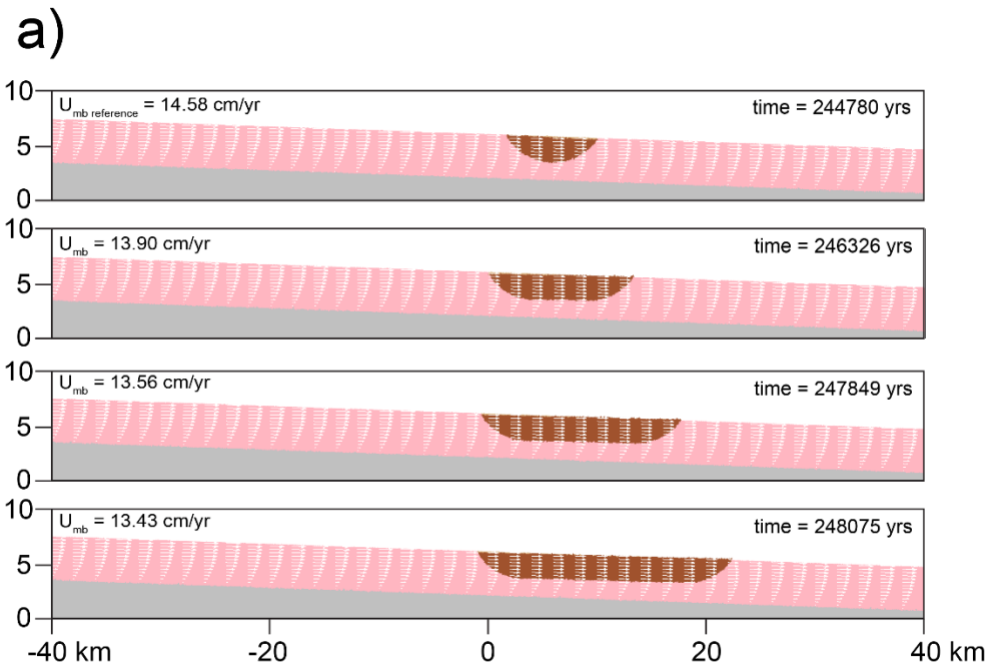

Figure SI-9. a) Screenshots at the same time-step of four simulations with neutral-density minibasins of same initial thickness but different length or aspect ratio. The minibasin to salt thickness of this example is T_{mb}/H_{salt} = 0.575. The arrow indicates the center of the minibasin, which at the beginning of the simulations was located at the same position for all for cases. The arrow at this time step illustrates, that although there has been differential translation, the amount is relatively small. The longest minibasin, which has the highest aspect ratio, (lower panel) has the slowest mean velocity of all, although the differences are relatively small.

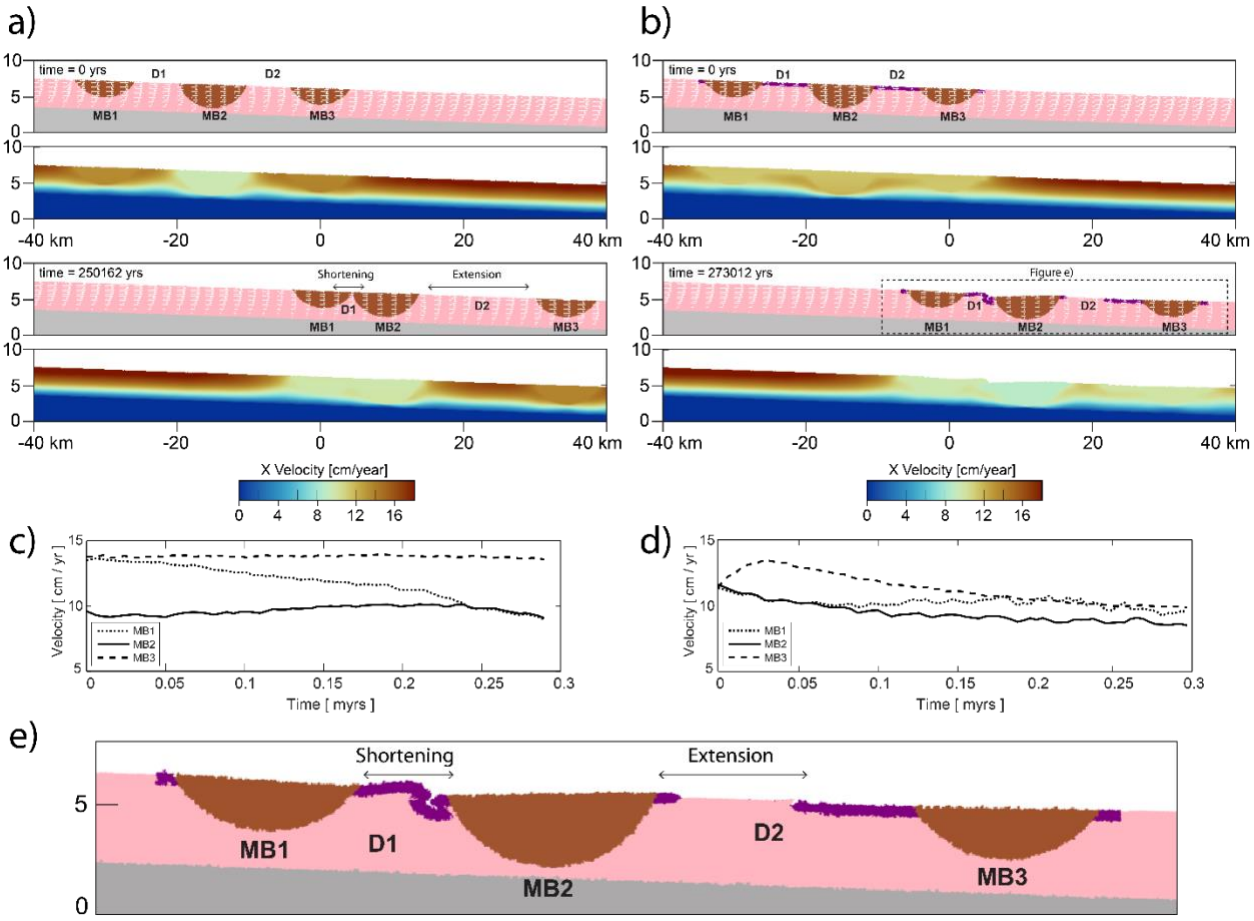

Figure SI-10. Screenshots of a three time-step evolution of a chain of three neutral-density minibasins on a slope (from updip to downdip, MB1, MB2 and M3; with intervening diapirs D1 and D2). The minibasin in the center (MB2) is thicker than the ones updip and downdip. Two scenarios are shown. One scenario in which the diapirs are exposed and not covered by a roof (a), and one in which the diapirs are covered by a roof on top (b). The velocities of the minibasins for each scenario are plotted in c) and d). In the simulation with the exposed diapirs (a), as the numerical simulation evolves, the thin minibasins (MB1 and MB3) translate faster than the thick minibasin (MB2) (c). However, as the simulation evolves, updip thin minibasin (MB1), decreases its velocity as it approaches the thick minibasin MB2 (c). In the simulation with covered diapirs (b), because the three minibasins are initially connected by the roof, their starting velocities are the same (d). However, as the simulation evolves, the downdip minibasin (MB3) drifts away from the minibasin in the center (MB2), the roof in between the two gets stretched (b, d). Instead, the minibasin updip (MB1), converges towards the minibasin in the center and the roof in between gets shortened by folding (b, c). e) Zoomed view of the rectangle of Figure b) where the deformation of the roof above the diapirs can be observed.

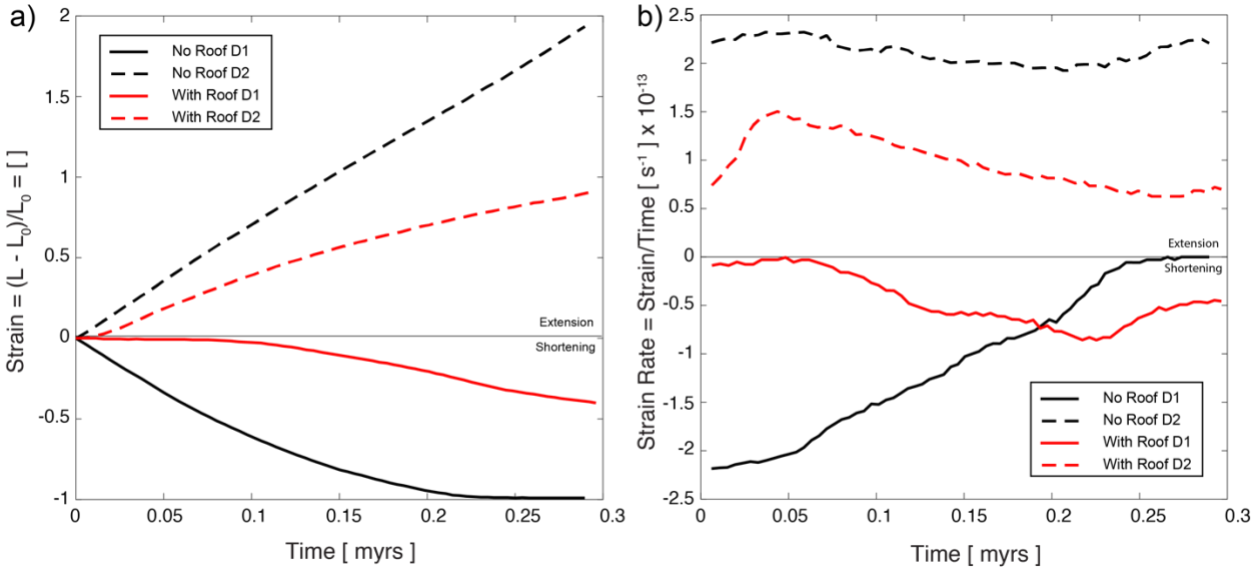

Figure SI-11. a) Strain accommodated by the diapirs D1 and D2, for the simulations with no roof and without roof. D1 is the diapir located upslope, in between the converging minibasins MB1 and MB2. As such, diapir D1 accommodates the shortening, as shown by negative value of the strain. The opposite is true for diapir D2, which is located downslope, between diverging minibasins MB2 and MB3. It must also be noted, the higher amount of strain, whether extensional or compressional, accommodated by the case in which the diapir has no roof. b) Strain rate calculated for the diapirs D1 and D2. The negative value of the strain rate indicates the shortening which is being accommodated by diapir D1. Notice, how in the case of the diapir with roof, the strain rate remains close to zero initially, meaning that there is no strain being accommodated by the roof. This is very different to what it is observed in the case with roof. Additionally, in the case of the diapir D2, both the cases with roof and no-roof start accommodating the deformation early in their evolution.